

Integral Micromorphic Model Reproducing Dispersion in 1D Continuum

Michal Šmejkal^{a,*}, Milan Jirásek^a, Martin Horák^{a,b}

^aCzech Technical University in Prague, Faculty of Civil Engineering, Department of Mechanics, Thákurova 2077/7, 166 29 Prague 6, Czechia

^bCzech Academy of Sciences, Institute of Information Theory and Automation, Pod vodárenskou věží 4, 182 00 Prague 8, Czechia

Abstract

The paper develops a new integral micromorphic elastic continuum model, which can describe dispersion properties of band-gap metamaterials, i.e., metamaterials that inhibit propagation of waves in a certain frequency range. The enrichment consists in nonlocal treatment of three terms in the expression for the potential energy density of the standard micromorphic continuum. After proper calibration, such a formulation can **exactly** reproduce two given branches of the dispersion curve (acoustic and optical), even in cases with a band gap. The calibration process exploits Fourier images of the unknown weight functions, which are analytically deduced from the dispersion relation of the material of interest. The weight functions are then reconstructed in the spatial domain by numerical evaluation of the inverse Fourier transform. The presented approach is validated on several examples, including discrete mass-spring chains with alternating masses, for which the dispersion relation has an explicit analytical form and the optical and acoustic branches are separated by a band gap.

Keywords: Micromorphic model, nonlocal continuum, dispersion, band gap

1. Introduction

1.1. Background

Over the past few years, there has been growing interest in mechanical metamaterials, stimulated by their ability to exhibit unique and customized properties. These materials are typically constructed using repeating unit cells arranged in a specific pattern. The advancement of 3D printing techniques has played a crucial role in developing and producing metamaterials, offering an efficient and reproducible manufacturing method [1, 2]. Among the various types of metamaterials, the Locally Resonant Acoustic Metamaterial (LRAM) has received significant attention [3, 4, 5]. LRAM exhibits a dispersion curve with multiple branches, known as the acoustic and optical branches, which are separated by a band gap. As a result, LRAM can effectively attenuate acoustic waves within a specific frequency range. This unique property opens up numerous possibilities for engineering applications, including acoustic cloaking, acoustic filters, and vibration isolation control [6, 7].

The development of metamaterials heavily relies on the availability of efficient and reliable computational tools that enable numerical simulation of their behavior and properties. One commonly used technique is direct numerical simulation, typically based on the finite element method, which takes into account the complete microstructure of the material. However, when dealing with large metamaterial structures, the computational costs associated with representing each unit cell's geometric details can quickly become prohibitive, making direct numerical simulations impractical for engineering applications. To address this challenge, homogenization techniques tailored to capture the behavior of Locally Resonant Acoustic Metamaterials have been developed, see, e.g., [8, 9, 10].

In addition to homogenization methods, various phenomenological theories have been proposed to incorporate the influence of material microstructure on the macroscopic behavior, e.g., on wave propagation. Extended continuum theories, such as higher-gradient elasticity [11, 12] and integral-type nonlocal elasticity [13, 14], have been introduced

*Corresponding author

Email addresses: michal.smejkal@fsv.cvut.cz (Michal Šmejkal), milan.jirasek@cvut.cz (Milan Jirásek), martin.horak@cvut.cz (Martin Horák)

as approaches to account for the effects of microstructure. A comprehensive investigation of dispersion properties for various integral- and gradient-type elasticity theories was presented in [15]. Even though gradient and integral continuum enrichments can model dispersive behavior, their dispersion diagrams have only a single branch. To capture the acoustic and optical branches in the dispersion diagram, an alternative approach is to utilize the micromorphic theory [16, 17]. Micromorphic continua introduce additional degrees of freedom that describe the deformation of the microstructure and offer a more comprehensive representation. However, classical micromorphic continua, including well-known models such as the Cosserat continuum [18, 19], microstretch continuum [20, 21], and full micromorphic continuum [16, 22], are unable to capture the band-gap phenomenon, as demonstrated in [23]. Furthermore, a detailed analysis of wave propagation in one-dimensional micromorphic continua, presented in [22], did not report any band gap. A one-dimensional micromorphic model with two internal variables was studied in [24], and it was demonstrated that this formulation can capture the band-gap phenomenon. In the variational derivation of the model, the kinetic energy density was constructed using a non-positive-definite mass matrix supplemented by a gyroscopic term, which enables the presence of multiple branches in the dispersion curve. In the conclusions, the authors pointed out that the mass matrix must be positive definite, and they left the removal of this deficiency for future investigations.

Recently, a novel relaxed micromorphic continuum has been introduced to effectively capture the band-gap phenomenon [25]. Extensive research on this continuum model has been conducted in a series of papers, see, e.g., [26, 27, 28, 29, 30, 31]. However, it is important to note that in one-dimensional scenarios, the micromorphic effects of the relaxed micromorphic continuum vanish since they describe relative rotations between the microstructure and the macroscopic matrix. In [23], the authors claimed that the relaxed micromorphic model was the only nonlocal continuum model capable of describing band gaps. Nevertheless, in a subsequent study [29], the same authors demonstrated that by incorporating a term with mixed temporal and spatial derivatives of displacement, classical micromorphic models could also account for the band-gap phenomenon.

A micromorphic model with a mixed temporal-spatial derivative of the micromorphic variable, developed based on microstructural arguments, was proposed for modeling band gaps in [32]. In addition, the so-called Maxwell-Rayleigh model [33] was shown to simulate band gaps, with experimental verification in [34]. This model possesses an appealing physical background. However, it only introduces an enhancement in the inertia term and does not consider the effects of higher-order gradients on the potential energy. Consequently, it cannot predict size effects typically observed in materials with microstructure.

Recently, a new micromorphic integral model was proposed in [35], which combines the micromorphic continuum theory with nonlocal integral averaging. This model can represent two branches of the dispersion curve separated by a band gap. Furthermore, it was shown in [35] that, for the standard local micromorphic continuum in 1D, a band gap appears only when the micromorphic modulus vanishes, i.e., in the particular case when the kinetic energy is enriched by a term dependent on the rate of the micromorphic variable and the potential energy by a penalty term that forces the micromorphic variable to remain close to the local strain but **not** by a term dependent on the spatial gradient of the micromorphic variable. Moreover, the authors showed that, in this special case, the micromorphic model leads to the same one-dimensional dispersion relation as the Maxwell-Rayleigh model in the form presented in [33]. Both models also share another feature: under static conditions, they reduce to the standard elastic continuum.

Furthermore, the authors of [36] obtained a different version of the Maxwell-Rayleigh-type model by heuristic homogenization of a one-dimensional mass-spring chain with internal resonators. Such a model also leads to a band gap in the dispersion curve, tunable by two parameters. This approach can be classified as a subclass of continualization methods [37]. In the standard formulation, either the equations of motion or the Lagrange functional describing a specific discrete structure are transformed into their continuum counterparts by approximating the displacement difference of neighboring particles by a truncated Taylor expansion of a continuous macro displacement field, leading to variants of gradient continuum models. However, due to the truncation of the Taylor expansion, the resulting continuum potential energy density functional might lose positive definiteness, leading to a mathematically ill-posed problem. Therefore, enhanced continualization schemes were developed to tackle such pathological effects. For instance, the authors of [38] introduced a regularized continualization technique preserving positive definiteness of the potential energy density functional for one-dimensional beam lattices and further generalized the procedure to multi-dimensional beam-like lattices [39] and to block-lattice materials [40]. By considering an increasing number of terms in the expansion, a gradient continuum of increasing order can be obtained, leading to a better match of the dispersion properties of the discrete lattice and the corresponding enriched continuum model. In the limit case, when infinitely many terms are considered in the expansion series, the resulting equations of motions can alternatively be obtained

from an integral-type continuum with a specific averaging kernel, and the dispersion properties of such an enriched continuum model would be identical to those of the analyzed discrete structure.

In the present paper, we propose an enriched continuum model that combines the nonlocal integral continuum theory with the micromorphic approach. This model is able to **exactly** reproduce the dispersive behavior of an arbitrary metamaterial with two branches in the dispersion diagram, including cases in which the branches are separated by a band gap. For calibration of the averaging kernels, only the knowledge of the standard macroscopic material parameters and of the dispersion relation of the analyzed material is needed. This is a novelty compared to the attempts to capture the band gap found in the literature, which either provide only an approximation of the dispersion relation, or require the knowledge of the microstructure (e.g., in the continualization methods). The whole paper is dedicated exclusively to infinite domains; therefore, the question of suitable boundary conditions for finite domains is left open for future research. Similarly, wave attenuation caused by damping is not considered in this work. In [41] the author studied wave dispersion and attenuation for various visco-elastic models enriched by gradient extensions. A similar analysis could also be performed for the micromorphic and integral extensions presented in this paper, but this remains to be explored in the future.

1.2. Motivation

In the present work, we build upon the results obtained with the micromorphic integral model introduced in [35] and propose its further generalization. Nonlocal averaging is now applied to all three free energy density function terms, i.e., the strain-related term, the micromorphic gradient term, and the coupling term. Each of the three nonlocal weight functions is then determined based on the given dispersion relation of the material to be reproduced. It turns out that by properly adjusting the weight functions, the present enriched continuum model can be tuned up to reproduce an arbitrary one-dimensional dispersion diagram consisting of two branches.

The developed identification procedure will be validated on three simple test cases for which the dispersion relation is available in an explicit analytical form. These examples will start from a discrete mass-spring chain with two alternating masses—perhaps one of the simplest discrete models showing a band gap in the dispersion curve. The second example will look at the micromorphic continuum with a vanishing micromorphic modulus, which is the only case of the standard 1D micromorphic continuum model that leads to a band gap. Finally, a mass-spring chain with two alternating masses and second-nearest-neighbor interactions will be considered. Based on the provided dispersion relations, the appropriate weight functions of the proposed micromorphic integral continuum will be constructed. The error will be assessed by comparison of the originally given dispersion relations with those obtained based on the present model. For simplicity, and to allow for analytical derivations as much as possible, the present study will be performed in the one-dimensional setting.

Before diving into the derivation of the model, we outline the line of reasoning and motivate the proposed form of the potential and kinetic energies. In [32], using micro-mechanical arguments, the authors developed a micromorphic model with a *mixed temporal-spatial derivative of the micromorphic variable*, governed by equations of motion

$$\rho \ddot{u}(x, t) = (\bar{E} + \bar{H}) u''(x, t) - \bar{H} \chi'(x, t) \quad (1)$$

$$\eta \ddot{\chi}(x, t) - C \dot{\chi}''(x, t) = \bar{A} \chi''(x, t) - \bar{H} \chi(x, t) + \bar{H} u'(x, t) \quad (2)$$

Here, x is the spatial coordinate and t is the time, primes denote spatial derivatives and overdots time derivatives, $u(x, t)$ is the macroscopic displacement field and $\chi(x, t)$ is the micromorphic variable field, which has the physical meaning of micro-level deformation, ρ is the macroscopic mass density, η and C stand for nonstandard micromorphic density measures, which can be computed based on the given microscopic density field, \bar{E} denotes the elastic modulus, and \bar{A} and \bar{H} are additional micromorphic stiffness parameters.

In a subsequent study [29], another micromorphic model incorporating a *mixed temporal and spatial derivative of the displacement field* was proposed and analyzed. The governing equations of that model read

$$\rho \ddot{u}(x, t) - B \ddot{u}''(x, t) = (\bar{E} + \bar{H}) u''(x, t) - \bar{H} \chi'(x, t) \quad (3)$$

$$\eta \ddot{\chi}(x, t) = \bar{A} \chi''(x, t) - \bar{H} \chi(x, t) + \bar{H} u'(x, t) \quad (4)$$

where B is an additional material parameter. Interestingly, both enhanced micromorphic models, i.e., model (1)–(2) with a mixed derivative of the micromorphic variable χ and model (3)–(4) with a mixed derivative of displacement u ,

symbol	meaning
x, ξ	space coordinates
$r = x - \xi $	spatial distance of points x and ξ
t	time coordinate
\bar{E}	elastic modulus
ρ	mass density
η	micromorphic density
$\tau = \sqrt{\eta/\bar{E}}$	characteristic time
$l = \sqrt{\eta/\rho}$	characteristic length
$\tilde{r} = r/l$	dimensionless distance
i	imaginary unit
k	wave number
$\tilde{k} = lk$	dimensionless wave number
ω	circular frequency
ω_1, ω_2	circular frequency of acoustic and optical branch
$\tilde{\omega} = \tau\omega$	dimensionless circular frequency
u	displacement field
\hat{u}	amplitude of harmonic displacement field
χ	micromorphic variable field
$\hat{\chi}$	amplitude of harmonic micromorphic strain field
\bar{H}	coupling stiffness
\bar{A}	micromorphic stiffness
$l_s = \sqrt{\bar{A}/\bar{E}}$	characteristic length related to stiffness
$\kappa = \bar{H}/\bar{E}$	ratio of coupling micromorphic stiffness and the standard stiffness
B, C	additional material parameters
Ψ	free energy
$\bar{\Psi}$	spatially averaged free energy
$\bar{\Psi}_E, \bar{\Psi}_A, \bar{\Psi}_H$	contributions of the standard, micromorphic, and coupling terms to spatially averaged free energy
T	kinetic energy
\bar{T}	spatially averaged kinetic energy
$\bar{T}_\rho, \bar{T}_\eta$	standard and micromorphic contributions to spatially averaged kinetic energy
S	action functional
E, A, H_1, H_2	weight functions
$E_s, A_s, H_{1,s}, H_{2,s}$	symmetrized weight functions
$E_0, A_0, H_{1,0}, H_{2,0}$	weight functions dependent only on a single variable (distance)
$\mathcal{E}, \mathcal{A}, \mathcal{H}_1, \mathcal{H}_2$	Fourier images of weight functions $E_0, A_0, H_{1,0}, H_{2,0}$
\mathcal{H}	Fourier image of weight function $H_{1,0} = H_{2,0}$
$\tilde{E}, \tilde{A}, \tilde{H}$	dimensionless weight functions
$\tilde{\mathcal{E}}, \tilde{\mathcal{A}}, \tilde{\mathcal{H}}$	dimensionless version of Fourier images $\mathcal{E}, \mathcal{A}, \mathcal{H}$
$\gamma = \tilde{\mathcal{A}}/\tilde{\mathcal{E}}$	ratio of dimensionless Fourier images $\tilde{\mathcal{A}}$ and $\tilde{\mathcal{E}}$
m, M	masses of the mass-spring chain
$\beta = m/M$	ratio of the masses m and M
K, K_1, K_2	stiffnesses of the mass-spring chains
$\xi = K_2/K_1$	stiffness ratio of the mass-spring chain with second-nearest-neighbour interactions
a	mass-spring chain particle distance
$\lambda = l/a$	ratio of characteristic length and particle distance
\tilde{k}_0	length of the sampling interval of the discrete Fourier transform
N	number of sampling points of the discrete Fourier transform
h	spacing in the space domain of the discrete Fourier transform
ϕ_j, Φ_j	j -th hat function and its Fourier transform

Table 1: List of symbols

lead to a band gap in the dispersion diagram. Note that the introduction of mixed derivatives can be traced back to [12], where a higher-order mathematical homogenization theory was used to derive a nonlocal dispersive model with mixed temporal and spatial derivatives of the displacement for wave propagation in heterogeneous materials.

It is now straightforward to combine both above-mentioned models into a generalized micromorphic model with mixed temporal and spatial derivatives of the displacement and micromorphic fields, described by equations of motion

$$\rho \ddot{u}(x, t) - B \ddot{u}'(x, t) = (\bar{E} + \bar{H}) u''(x, t) - \bar{H} \chi'(x, t) \quad (5)$$

$$\eta \ddot{\chi}(x, t) - C \ddot{\chi}''(x, t) = \bar{A} \chi''(x, t) - \bar{H} \chi(x, t) + \bar{H} u'(x, t) \quad (6)$$

However, for this kind of model, the dispersion diagram has certain features encoded in the formulation, which cannot be changed even if the material parameters are adjusted. For example, this model cannot capture the dispersion diagram of the double-mass-spring model, which is one of the simplest one-dimensional cases that exhibit a band gap.

Based on ideas from [15], differential equations (5)–(6) may alternatively be reformulated in the integral form

$$\rho \ddot{u}(x, t) = (\bar{E} + \bar{H}) \int_{\mathcal{L}} G_1(x, \xi) u''(\xi, t) d\xi - \bar{H} \int_{\mathcal{L}} G_1(x, \xi) \chi'(\xi, t) d\xi \quad (7)$$

$$\eta \ddot{\chi}(x, t) = \bar{A} \int_{\mathcal{L}} G_2(x, \xi) \chi''(\xi, t) d\xi + \bar{H} \int_{\mathcal{L}} G_2(x, \xi) u'(\xi, t) d\xi - \bar{H} \int_{\mathcal{L}} G_2(x, \xi) \chi(\xi, t) d\xi \quad (8)$$

in which \mathcal{L} is the one-dimensional spatial domain (interval) on which the problem is solved, and $G_1(x, \xi)$ and $G_2(x, \xi)$ denote the Green functions of the spatial differential operators that convert the left-hand sides of (7) and (8) into the left-hand sides of (5) and (6), respectively, i.e., of operators $\mathcal{I} - (B/\rho) \partial^2 / \partial^2 x$ and $\mathcal{I} - (C/\rho) \partial^2 / \partial^2 x$ where \mathcal{I} is the identity operator. Equations of motion (7)–(8) are taken as the starting point and further generalized by replacing the Green functions G_1 and G_2 by arbitrary averaging kernels, which enhances the flexibility of the model.

2. General One-Dimensional Integral Micromorphic Model

2.1. Model formulation

Instead of directly postulating a generalized form of equations of motion (7)–(8), we will use an energy-based approach. For a standard (local) micromorphic model, the free energy is expressed as

$$\Psi = \int_{\mathcal{L}} \left(\frac{1}{2} \bar{E} u'^2(x) + \frac{1}{2} \bar{A} \chi'^2(x) + \frac{1}{2} \bar{H} (u'(x) - \chi(x))^2 \right) dx \quad (9)$$

where the first term in the integrand represents the energy stored in strain, the second term is the energy stored in the gradient of micromorphic strain, and the third term penalizes the difference between the strain evaluated from the displacement field and the micromorphic strain.

The newly proposed nonlocal version of the micromorphic model defines the free energy as

$$\begin{aligned} \Psi(t) = & \int_{\mathcal{L}} \frac{1}{2} \left(\int_{\mathcal{L}} E(x, \xi) u'(\xi, t) d\xi \right) u'(x, t) dx + \int_{\mathcal{L}} \frac{1}{2} \left(\int_{\mathcal{L}} A(x, \xi) \chi'(\xi, t) d\xi \right) \chi'(x, t) dx + \\ & + \int_{\mathcal{L}} \frac{1}{2} \left(\int_{\mathcal{L}} (H_1(x, \xi) u'(\xi, t) - H_2(x, \xi) \chi(\xi, t)) d\xi \right) (u'(x, t) - \chi(x, t)) dx \end{aligned} \quad (10)$$

where $E(x, \xi)$, $A(x, \xi)$, $H_1(x, \xi)$ and $H_2(x, \xi)$ are suitable weight functions, and it is marked explicitly that the displacement, micromorphic strain and free energy vary in time. The kinetic energy

$$T(t) = \int_{\mathcal{L}} \left(\frac{1}{2} \rho \dot{u}(x, t)^2 + \frac{1}{2} \eta \dot{\chi}(x, t)^2 \right) dx \quad (11)$$

consists of a standard term related to the displacement rate and a micromorphic enhancement related to the rate of the micromorphic strain. We are interested in the structure of the governing equations and, for simplicity, we assume that the weight functions as well as the kinematic fields are sufficiently regular, so that all integrals involved in the

subsequent derivations remain finite. Also, \mathcal{L} should be understood as a finite interval in all intermediate steps, but the resulting equations can be extended to the whole real axis by a limit process.

In the spirit of the Hamilton principle, let us define the action functional

$$\mathcal{S} = \int_{t_1}^{t_2} (T(t) - \Psi(t)) dt \quad (12)$$

and set its first variation to zero, assuming that the state of the system at times t_1 and t_2 is fixed. Substituting from (10)–(11), evaluating the variation $\delta\mathcal{S}$, integrating by parts with respect to time (to convert the rates of variations δu and $\delta\chi$ into the variations), and taking into account that the variations δu and $\delta\chi$ at t_1 and t_2 vanish, we obtain the stationarity condition

$$- \int_{\mathcal{L}} [\rho\ddot{u}(x, t)\delta u(x, t) + \eta\ddot{\chi}(x, t)\delta\chi(x, t) + \Sigma(x, t)\delta u'(x, t) dx + \Theta_0(x, t)\delta\chi(x, t) dx + \Theta_1(x, t)\delta\chi'(x, t)] dx = 0 \quad (13)$$

in which

$$\begin{aligned} \Sigma(x, t) &= \int_{\mathcal{L}} (E_s(x, \xi) + H_{1,s}(x, \xi))u'(\xi, t) d\xi - \frac{1}{2} \int_{\mathcal{L}} (H_2(x, \xi) + H_1(\xi, x))\chi(\xi, t) d\xi \\ \Theta_0(x, t) &= \int_{\mathcal{L}} H_{2,s}(x, \xi)\chi(\xi, t) d\xi - \frac{1}{2} \int_{\mathcal{L}} (H_1(x, \xi) + H_2(\xi, x)) u'(\xi, t) d\xi \\ \Theta_1(x, t) &= \int_{\mathcal{L}} A_s(x, \xi)\chi'(\xi, t) d\xi \end{aligned}$$

The added subscript s denotes symmetrization with respect to coordinates x and ξ , i.e., for a general function $f(x, \xi)$ we define $f_s(x, \xi) = \frac{1}{2}(f(x, \xi) + f(\xi, x))$.

In the next step, let us integrate (13) by parts with respect to the spatial coordinate x (to convert the spatial derivatives of variations into the variations), and take into account the independence of variations δu and $\delta\chi$. The resulting strong form of the equations of motion reads

$$\rho\ddot{u}(x, t) = \left(\int_{\mathcal{L}} (E_s(x, \xi) + H_{1,s}(x, \xi))u'(\xi, t) d\xi - \frac{1}{2} \int_{\mathcal{L}} (H_2(x, \xi) + H_1(\xi, x))\chi(\xi, t) d\xi \right)' \quad (14)$$

$$\eta\ddot{\chi}(x, t) = \left(\int_{\mathcal{L}} A_s(x, \xi)\chi'(\xi, t) d\xi \right)' + \frac{1}{2} \int_{\mathcal{L}} (H_1(x, \xi) + H_2(\xi, x)) u'(\xi, t) d\xi - \int_{\mathcal{L}} H_{2,s}(x, \xi)\chi(\xi, t) d\xi \quad (15)$$

If $\mathcal{L} = (-\infty, \infty)$ and the weight functions depend only on the distance, i.e., if $E(x, \xi) = E_0(x-\xi)$, $A(x, \xi) = A_0(x-\xi)$, $H_1(x, \xi) = H_{1,0}(x-\xi)$ and $H_2(x, \xi) = H_{2,0}(x-\xi)$ where all functions with subscript 0 are even, then the “outer derivative” on the right-hand sides of (14) and (15) can be “shifted” into the nonlocal integrals. The procedure is demonstrated for the first term on the right-hand side of (14):

$$\begin{aligned} \left(\int_{\mathcal{L}} E_0(x-\xi)u'(\xi, t) d\xi \right)' &= \int_{\mathcal{L}} E_0'(x-\xi)u'(\xi, t) d\xi = - \int_{\mathcal{L}} E_0'(\xi-x)u'(\xi, t) d\xi = \\ &= - [E_0(\xi-x)u'(\xi, t)]_{\xi=-\infty}^{\infty} + \int_{\mathcal{L}} E_0(\xi-x)u''(\xi, t) d\xi = \int_{\mathcal{L}} E_0(x-\xi)u''(\xi, t) d\xi \end{aligned} \quad (16)$$

Here we have assumed that the weight functions tend to zero as the interaction distance increases, e.g., $E_0(r) \rightarrow 0$ as $|r| \rightarrow \infty$. The remaining terms can be simplified in an analogous way, and equations (14) and (15) can be rewritten as

$$\rho\ddot{u}(x, t) = \int_{\mathcal{L}} (E_s(x, \xi) + H_{1,s}(x, \xi))u''(\xi, t) d\xi - \frac{1}{2} \int_{\mathcal{L}} (H_2(x, \xi) + H_1(\xi, x))\chi'(\xi, t) d\xi \quad (17)$$

$$\eta\ddot{\chi}(x, t) = \int_{\mathcal{L}} A_s(x, \xi)\chi''(\xi, t) d\xi + \frac{1}{2} \int_{\mathcal{L}} (H_1(x, \xi) + H_2(\xi, x)) u'(\xi, t) d\xi - \int_{\mathcal{L}} H_{2,s}(x, \xi)\chi(\xi, t) d\xi \quad (18)$$

$$\rho \ddot{u}(x, t) = \int_{\mathcal{L}} (E_0(x - \xi) + H_{1,0}(x - \xi)) u''(\xi, t) d\xi - \frac{1}{2} \int_{\mathcal{L}} (H_{2,0}(x - \xi) + H_{1,0}(\xi - x)) \chi'(\xi, t) d\xi \quad (19)$$

$$\eta \ddot{\chi}(x, t) = \int_{\mathcal{L}} A_0(x - \xi) \chi''(\xi, t) d\xi + \frac{1}{2} \int_{\mathcal{L}} (H_{1,0}(x - \xi) + H_{2,0}(\xi - x)) u'(\xi, t) d\xi - \int_{\mathcal{L}} H_{2,0}(x - \xi) \chi(\xi, t) d\xi \quad (20)$$

Comparing the resulting equations of motion (19)–(20) with eqs. (7)–(8) derived from the micromorphic continuum model with mixed derivatives, it is apparent that their structure is very similar. Both formulations can be made equivalent (on an infinite domain) if the parameters in (5)–(6) satisfy condition $B/\rho = C/\eta$, which leads to identical Green functions that can be presented in the form $G_i(x, \xi) = G_0(x - \xi)$, $i = 1, 2$. It is then sufficient to set $H_{1,0}(r) = H_{2,0}(r) = \bar{H} G_0(r)$, $A(r) = \bar{A} G_0(r)$ and $E(r) = \bar{E} G_0(r)$. In general, the weight functions can have different forms, which makes the proposed integral formulation more flexible, leading to a rich family of dispersion diagrams.

2.2. Dispersion relation

Let us consider solutions that have the form of a harmonic wave, described in the complex representation by

$$u(x, t) = \hat{u} e^{i(kx - \omega t)} \quad (21)$$

$$\chi(x, t) = \hat{\chi} e^{i(kx - \omega t)} \quad (22)$$

where \hat{u} and $\hat{\chi}$ are the amplitudes of displacement and micromorphic strain, k is the wave number, ω is the circular frequency, and $i = \sqrt{-1}$ is the imaginary unit. Substituting this ansatz into the equations of motion (19)–(20), we obtain, after some manipulations, a set of two homogeneous linear algebraic equations

$$\begin{pmatrix} [\mathcal{E}(k) + \mathcal{H}_1(k)] k^2 - \rho \omega^2 & \frac{1}{2} [\mathcal{H}_1(k) + \mathcal{H}_2(k)] ik \\ -\frac{1}{2} [\mathcal{H}_1(k) + \mathcal{H}_2(k)] ik & k^2 \mathcal{A}(k) + \mathcal{H}_2(k) - \eta \omega^2 \end{pmatrix} \begin{pmatrix} \hat{u} \\ \hat{\chi} \end{pmatrix} = \begin{pmatrix} 0 \\ 0 \end{pmatrix} \quad (23)$$

in which $\mathcal{E}(k)$, $\mathcal{A}(k)$, $\mathcal{H}_1(k)$ and $\mathcal{H}_2(k)$ are Fourier images of weight functions E_0 , A_0 , $H_{1,0}$ and $H_{2,0}$, resp., considered as dependent only on the distance $r = |x - \xi|$, which is a reasonable assumption in an infinite homogeneous body. For the present purpose, the Fourier transform $\mathcal{F}(E_0) = \mathcal{E}$ is defined by

$$\mathcal{E}(k) = \int_{-\infty}^{\infty} E_0(r) e^{-ikr} dr \quad (24)$$

and its inverse, $E_0 = \mathcal{F}^{-1}(\mathcal{E})$ is evaluated as

$$E_0(r) = \frac{1}{2\pi} \int_{-\infty}^{\infty} \mathcal{E}(k) e^{ikr} dk \quad (25)$$

Since the weight functions are real and even, their Fourier images are also real and even, and relations (24)–(25) can be written in their equivalent form

$$\mathcal{E}(k) = \int_{-\infty}^{\infty} E_0(r) \cos kr dr = 2 \int_0^{\infty} E_0(r) \cos kr dr \quad (26)$$

$$E_0(r) = \frac{1}{2\pi} \int_{-\infty}^{\infty} \mathcal{E}(k) \cos kr dk = \frac{1}{\pi} \int_0^{\infty} \mathcal{E}(k) \cos kr dk \quad (27)$$

The dependence of the Fourier images on the wave number k will not be marked in the subsequent derivation anymore.

Equations (23) have a nontrivial solution only if the determinant of the 2×2 matrix on the left-hand side vanishes. To simplify the analysis, let us assume that $H_1 = H_2$ and denote the corresponding Fourier image as \mathcal{H} . The condition of zero determinant then leads to

$$\rho \eta \omega^4 - (\rho(\mathcal{A}k^2 + \mathcal{H}) + \eta(\mathcal{E} + \mathcal{H})k^2) \omega^2 + \mathcal{A}(\mathcal{E} + \mathcal{H})k^4 + \mathcal{E}\mathcal{H}k^2 = 0 \quad (28)$$

This dispersion equation is quadratic in terms of ω^2 and may provide two positive values of circular frequency ω for each given positive wave number k . Note that \mathcal{E} , \mathcal{A} , and \mathcal{H} are functions of k . The problem can now be inverted: Suppose that two branches of the dispersion diagram are known and are described by functions $\omega_1(k)$ and $\omega_2(k)$, with $\omega_1(0) = 0$ (acoustic branch) and $\omega_2(0) > 0$ (optical branch). We are looking for appropriate weight functions, represented by their Fourier images, such that the dispersion equation be satisfied for each wave number k combined with the corresponding circular frequency $\omega_1(k)$, and also with $\omega_2(k)$. Functions \mathcal{E} , \mathcal{A} , and \mathcal{H} are now treated as unknowns, for which we can set up two equations (to be satisfied for all values of k):

$$\rho\eta\omega_1^4 - (\rho(\mathcal{A}k^2 + \mathcal{H}) + \eta(\mathcal{E} + \mathcal{H})k^2)\omega_1^2 + \mathcal{A}(\mathcal{E} + \mathcal{H})k^4 + \mathcal{E}\mathcal{H}k^2 = 0 \quad (29)$$

$$\rho\eta\omega_2^4 - (\rho(\mathcal{A}k^2 + \mathcal{H}) + \eta(\mathcal{E} + \mathcal{H})k^2)\omega_2^2 + \mathcal{A}(\mathcal{E} + \mathcal{H})k^4 + \mathcal{E}\mathcal{H}k^2 = 0 \quad (30)$$

In terms of \mathcal{E} , \mathcal{A} , and \mathcal{H} , these equations are nonlinear, but nonlinearity resides only in the terms independent of ω . When (29) is subtracted from (30), the resulting equation

$$\rho\eta(\omega_2^4 - \omega_1^4) - (\rho(\mathcal{A}k^2 + \mathcal{H}) + \eta(\mathcal{E} + \mathcal{H})k^2)(\omega_2^2 - \omega_1^2) = 0 \quad (31)$$

is linear (in terms of \mathcal{E} , \mathcal{A} , and \mathcal{H}), and it can be rewritten as

$$\rho(\mathcal{A}k^2 + \mathcal{H}) + \eta(\mathcal{E} + \mathcal{H})k^2 = \rho\eta(\omega_1^2 + \omega_2^2) \quad (32)$$

It is now easy to express

$$\mathcal{H} = \frac{\rho\eta(\omega_1^2 + \omega_2^2) - (\rho\mathcal{A} + \eta\mathcal{E})k^2}{\rho + \eta k^2} \quad (33)$$

and substitute back into (29), which yields a seemingly complicated equation

$$\rho\eta\omega_1^4 - (\rho\mathcal{A} + \eta\mathcal{E})k^2\omega_1^2 - (\rho + \eta k^2)\omega_1^2 \frac{\rho\eta(\omega_1^2 + \omega_2^2) - (\rho\mathcal{A} + \eta\mathcal{E})k^2}{\rho + \eta k^2} + \mathcal{A}\mathcal{E}k^4 + (\mathcal{A}k^2 + \mathcal{E})k^2 \frac{\rho\eta(\omega_1^2 + \omega_2^2) - (\rho\mathcal{A} + \eta\mathcal{E})k^2}{\rho + \eta k^2} = 0 \quad (34)$$

However, many terms cancel out and the equation can be simplified to

$$-\rho\eta(\rho + \eta k^2)\omega_1^2\omega_2^2 + \rho\eta(\omega_1^2 + \omega_2^2)(\mathcal{A}k^2 + \mathcal{E})k^2 - \rho\mathcal{A}^2k^6 - \eta\mathcal{E}^2k^4 = 0 \quad (35)$$

which is a quadratic equation with two unknowns, \mathcal{E} and \mathcal{A} . The mixed term with the product $\mathcal{E}\mathcal{A}$ is missing and the terms with \mathcal{E}^2 and \mathcal{A}^2 have coefficients of the same sign. Therefore, the set of all solutions is in the $\mathcal{E} - \mathcal{A}$ plane graphically represented by an ellipse with axes parallel to the coordinate axes.

A special case arises for $k = 0$, because many coefficients in (35) vanish and the equation reduces to the identity

$$-\rho^2\eta\omega_1^2(0)\omega_2^2(0) = 0 \quad (36)$$

which is always satisfied, since $\omega_1(0) = 0$. This means that the values of $\mathcal{E}(0)$ and $\mathcal{A}(0)$ are arbitrary, but the value of

$$\mathcal{H}(0) = \eta(\omega_2^2(0) + \omega_1^2(0)) = \eta\omega_2^2(0) \quad (37)$$

can be determined from (33) with k set to zero. This result indicates that the circular frequency on the optical branch at $k = 0$ is linked to the model parameters by

$$\omega_2(0) = \sqrt{\frac{\mathcal{H}(0)}{\eta}} \quad (38)$$

where

$$\mathcal{H}(0) = \int_{-\infty}^{\infty} H_0(r) dr \quad (39)$$

is the nonlocal counterpart of the coupling modulus \bar{H} from (9).

For very small wave numbers k , the terms with k^4 and k^6 can be neglected and (35) reduces to

$$-\rho\eta(\rho + \eta k^2)\omega_1^2\omega_2^2 + \rho\eta(\omega_1^2 + \omega_2^2)\mathcal{E}k^2 = 0 \quad (40)$$

Since ω_1 is expected to be of the order of k as $k \rightarrow 0^+$, we can neglect terms with $\omega_1^2 k^2$ and also approximate $\mathcal{E}(k) k^2$ by $\mathcal{E}(0) k^2$, neglecting terms with the third and higher powers of k . Equation (40) is then approximated by

$$-\rho^2\eta\omega_1^2\omega_2^2 + \rho\eta\omega_2^2\mathcal{E}(0)k^2 = 0 \quad (41)$$

from which

$$\omega_1(k) = \sqrt{\frac{\mathcal{E}(0)}{\rho}} k \quad (42)$$

Here,

$$\mathcal{E}(0) = \int_{-\infty}^{\infty} E_0(r) dr = \bar{E} \quad (43)$$

plays the role of the macroscopic elastic modulus, and $\sqrt{\mathcal{E}(0)/\rho}$ is the standard wave speed of long elastic waves, i.e., the theoretical limit approached by the wave speed as the wave length tends to infinity. Of course, (42) is only a first-order approximation of function $\omega_1(k)$ valid near $k = 0$.

2.3. Dimensionless form

To simplify further derivations, the relevant equations are cast into a dimensionless form. For easy reference, the dimensions of individual model parameters (including the weight functions) are shown in Table 2. By combining the

parameter/variable	ρ	η	$E_0(r)$	$H_0(r)$	$A_0(r)$	$\mathcal{E}(k), \bar{E}$	$\mathcal{H}(k), \bar{H}$	$\mathcal{A}(k), \bar{A}$
unit	kg/m ³	kg/m	kg/(m ² ·s ²)	kg/(m ² ·s ²)	kg/s ²	kg/(m·s ²)	kg/(m·s ²)	kg·m/s ²

Table 2: Parameters and their units

basic parameters, we can define a characteristic time, e.g., $\tau = \sqrt{\eta/\bar{E}}$, and a characteristic length, e.g., $l = \sqrt{\eta/\rho}$, and then transform the circular frequency ω into a dimensionless variable $\tilde{\omega} = \tau\omega$ and the wave number k into a dimensionless variable $\tilde{k} = lk$. The role of characteristic stress/modulus can be played by the macroscopic elastic modulus \bar{E} . The dimensionless counterparts of weight functions $E_0(r)$, $A_0(r)$, and $H_0(r)$ are defined as

$$\tilde{E}(\tilde{r}) = \frac{l}{\bar{E}} E_0(l\tilde{r}) \quad (44)$$

$$\tilde{A}(\tilde{r}) = \frac{1}{l\bar{E}} A_0(l\tilde{r}) \quad (45)$$

$$\tilde{H}(\tilde{r}) = \frac{l}{\bar{E}} H_0(l\tilde{r}) \quad (46)$$

where $\tilde{r} = r/l$ is the dimensionless distance, and their Fourier images are

$$\tilde{\mathcal{E}}(\tilde{k}) = \frac{1}{\bar{E}} \mathcal{E}(\tilde{k}/l) \quad (47)$$

$$\tilde{\mathcal{A}}(\tilde{k}) = \frac{1}{l^2\bar{E}} \mathcal{A}(\tilde{k}/l) \quad (48)$$

$$\tilde{\mathcal{H}}(\tilde{k}) = \frac{1}{\bar{E}} \mathcal{H}(\tilde{k}/l) \quad (49)$$

It is worth noting that, due to the choice of the normalizing factor \bar{E} , the value of $\tilde{\mathcal{E}}(0)$ is not arbitrary—it is always equal to 1. In fact, $\tilde{\mathcal{E}}(\tilde{k})$ is the Fourier image of the normalized weight function, which is then multiplied by the physical modulus to construct the actual weight function that represents the nonlocal stiffness.

After the replacement of all variables by their dimensionless counterparts, Equation (35) is reformulated in the dimensionless form

$$-(1 + \tilde{k}^2)\tilde{\omega}_1^2\tilde{\omega}_2^2 + (\tilde{\omega}_1^2 + \tilde{\omega}_2^2)(\tilde{\mathcal{A}}\tilde{k}^2 + \tilde{\mathcal{E}})\tilde{k}^2 - \tilde{\mathcal{A}}^2\tilde{k}^6 - \tilde{\mathcal{E}}^2\tilde{k}^4 = 0 \quad (50)$$

Recall that $\tilde{\mathcal{E}}$ and $\tilde{\mathcal{A}}$ are so far unknown functions of the dimensionless wave number \tilde{k} . For a given \tilde{k} , the set of pairs $[\tilde{\mathcal{E}}, \tilde{\mathcal{A}}]$ that satisfy (50) can be graphically represented by an ellipse in the $\tilde{\mathcal{E}} - \tilde{\mathcal{A}}$ space. This is best seen if equation (50) is rearranged into the standard form

$$\frac{\left(\tilde{\mathcal{A}} - \frac{\tilde{\omega}_1^2 + \tilde{\omega}_2^2}{2\tilde{k}^2}\right)^2}{\frac{(\tilde{\omega}_1^2 - \tilde{\omega}_2^2)^2(\tilde{k}^2 + 1)}{4\tilde{k}^6}} + \frac{\left(\tilde{\mathcal{E}} - \frac{\tilde{\omega}_1^2 + \tilde{\omega}_2^2}{2\tilde{k}^2}\right)^2}{\frac{(\tilde{\omega}_1^2 - \tilde{\omega}_2^2)^2(\tilde{k}^2 + 1)}{4\tilde{k}^4}} = 1 \quad (51)$$

from which one can identify that the center of the ellipse is located at $[\tilde{\mathcal{E}}, \tilde{\mathcal{A}}] = \left[\frac{\tilde{\omega}_1^2 + \tilde{\omega}_2^2}{2\tilde{k}^2}, \frac{\tilde{\omega}_1^2 + \tilde{\omega}_2^2}{2\tilde{k}^2}\right]$ and the length of its axes can be obtained by doubling the square roots of the denominators in (51). Moreover, the ratio of the lengths of the axes in the $\tilde{\mathcal{E}}$ and the $\tilde{\mathcal{A}}$ directions turns out to be equal to \tilde{k} . Since both denominators in (51) are always nonnegative, the solution exists for any positive wave number. In the special case when $\omega_1(k) = \omega_2(k)$ for some k , i.e., when the branches of the dispersion diagram intersect, the solution is unique (the ellipse degenerates into a single point), but in a general case there exist infinitely many pairs $[\tilde{\mathcal{E}}, \tilde{\mathcal{A}}]$ satisfying the equation. For each of them, it is possible to evaluate the corresponding dimensionless function $\tilde{\mathcal{H}}$ using the dimensionless version of (33):

$$\tilde{\mathcal{H}} = \frac{1}{\tilde{E}}\mathcal{H} = \frac{\tilde{\omega}_2^2 + \tilde{\omega}_1^2 - (\tilde{\mathcal{A}} + \tilde{\mathcal{E}})\tilde{k}^2}{1 + \tilde{k}^2} \quad (52)$$

2.4. Solution

In the foregoing derivation it has been shown that, for a given dispersion diagram with two distinct branches and any given wave number, there exist infinitely many solutions $\tilde{\mathcal{E}}(\tilde{k})$ and $\tilde{\mathcal{A}}(\tilde{k})$ which satisfy equation (51), derived from (35). The task is now to choose, for each \tilde{k} , one of the admissible solutions such that the resulting Fourier images of the weight functions, and the weight functions themselves, have meaningful properties.

To simplify the model and make the solution unique, let us enforce a constant ratio $\gamma = \tilde{\mathcal{A}}(\tilde{k})/\tilde{\mathcal{E}}(\tilde{k})$, which leads to $\tilde{\mathcal{A}}(k) = \gamma^2\tilde{\mathcal{E}}(k)$ and eventually to $A_0(r) = \gamma^2E_0(r)$, i.e., to weight functions of the same shape. If the relation $\tilde{\mathcal{A}}(\tilde{k}) = \gamma\tilde{\mathcal{E}}(\tilde{k})$ is substituted into equation (50), we obtain

$$-(\gamma^2\tilde{k}^6 + \tilde{k}^4)\tilde{\mathcal{E}}^2 + (\tilde{\omega}_1^2 + \tilde{\omega}_2^2)(\gamma\tilde{k}^2 + 1)\tilde{k}^2\tilde{\mathcal{E}} - (1 + \tilde{k}^2)\tilde{\omega}_1^2\tilde{\omega}_2^2 = 0 \quad (53)$$

This is a quadratic equation for the unknown weight function $\tilde{\mathcal{E}}$, which has two roots

$$\tilde{\mathcal{E}}_{1,2} = \frac{(\tilde{\omega}_1^2 + \tilde{\omega}_2^2)(\gamma\tilde{k}^2 + 1) \pm \sqrt{(\tilde{\omega}_1^2 + \tilde{\omega}_2^2)^2(\gamma\tilde{k}^2 + 1)^2 - 4(\gamma^2\tilde{k}^2 + 1)(1 + \tilde{k}^2)\tilde{\omega}_1^2\tilde{\omega}_2^2}}{2(\gamma^2\tilde{k}^4 + \tilde{k}^2)} \quad (54)$$

The proper root can be selected based on the condition $\tilde{\mathcal{E}}(0) = 1$, which originates from the scaling used in the definition of the dimensionless weight function $\tilde{E}(\tilde{r})$ and its Fourier image $\tilde{\mathcal{E}}(\tilde{k})$. For $\tilde{k} = 0$, the denominator of the fraction in (54) is zero, and the fraction can have a finite limit at $\tilde{k} \rightarrow 0$ only if the numerator vanishes as well. The numerator evaluated for $\tilde{k} = 0$ reduces to $\tilde{\omega}_1^2 + \tilde{\omega}_2^2 \pm |\tilde{\omega}_2^2 - \tilde{\omega}_1^2|$. If $\tilde{\omega}_1$ corresponds to the acoustic branch and $\tilde{\omega}_2$ to the optical branch, i.e., if $\tilde{\omega}_1(0) = 0$ and $\tilde{\omega}_2(0) > 0$, the numerator equals $\tilde{\omega}_2^2 \pm \tilde{\omega}_2^2$, which vanishes if the negative sign is used. Therefore, to ensure continuity, we select the smaller root (even if \tilde{k} is arbitrary) and write the unique solution as

$$\tilde{\mathcal{E}} = \frac{(\tilde{\omega}_1^2 + \tilde{\omega}_2^2)(\gamma\tilde{k}^2 + 1) - \sqrt{(\tilde{\omega}_1^2 + \tilde{\omega}_2^2)^2(\gamma\tilde{k}^2 + 1)^2 - 4(\gamma^2\tilde{k}^2 + 1)(1 + \tilde{k}^2)\tilde{\omega}_1^2\tilde{\omega}_2^2}}{2(\gamma^2\tilde{k}^4 + \tilde{k}^2)} \quad (55)$$

However, the selection of the smaller root only makes sure that the numerator vanishes at $\tilde{k} = 0$ and the fraction becomes of the 0/0 type, but it is not yet guaranteed that the fraction tends to 1 as $\tilde{k} \rightarrow 0$. Detailed analysis based

on the L'Hospital rule reveals that the limit value of the fraction is $(d\tilde{\omega}_1(0)/d\tilde{k})^2$ and the normalizing condition is satisfied only if $d\tilde{\omega}_1(0)/d\tilde{k} = 1$. This is closely related to the fact that the present choice of characteristic time and characteristic length leads to a unit speed of long elastic waves in the dimensionless representation.

Once function $\tilde{\mathcal{E}}$ has been determined, it is straightforward to evaluate the corresponding $\tilde{\mathcal{A}} = \gamma\tilde{\mathcal{E}}$ and, based on (52), also

$$\tilde{\mathcal{H}} = \frac{\tilde{\omega}_1^2 + \tilde{\omega}_2^2}{1 + \tilde{k}^2} - (1 + \gamma) \frac{\tilde{k}^2}{1 + \tilde{k}^2} \tilde{\mathcal{E}} \quad (56)$$

Subsequently, the dimensionless wave number \tilde{k} is replaced by the product lk , and simple scaling leads to the “true” Fourier images $\mathcal{E} = \tilde{E}\tilde{\mathcal{E}}$, $\mathcal{A} = l^2\tilde{E}\tilde{\mathcal{E}}$ and $\mathcal{H} = \tilde{E}\tilde{\mathcal{H}}$. Finally, the inverse Fourier transform yields the weight functions E_0 , A_0 , and H_0 in the physical space.

As the weight functions are supposed to be real functions of the distance $|x - \xi|$, and thus even functions of the difference $x - \xi$, their Fourier images should also be real functions. The outlined procedure may not always give physically meaningful results since the discriminant of quadratic equation (53) may become negative. Graphically, this means that the ellipse in the $(\mathcal{E}, \mathcal{A})$ space may have no intersection with the straight line of selected slope γ . Interestingly, for the particular choice of $\gamma = 1$, the discriminant is always nonnegative and, moreover, the solution greatly simplifies and formulae (55)–(56) reduce to

$$\tilde{\mathcal{E}} = \frac{\tilde{\omega}_1^2}{\tilde{k}^2} \quad (57)$$

$$\tilde{\mathcal{H}} = \frac{\tilde{\omega}_2^2 - \tilde{\omega}_1^2}{1 + \tilde{k}^2} \quad (58)$$

Here we consider that the subscripts are assigned such that $\tilde{\omega}_1 \leq \tilde{\omega}_2$.

In general, a fixed straight line of slope γ has intersections with all the ellipses in the $(\mathcal{E}, \mathcal{A})$ space that correspond to all possible values of $\tilde{k} \geq 0$ only if γ is selected in a certain range. The limiting slopes can be found from the condition of zero discriminant of (53), which is in terms of γ again a quadratic equation

$$\left(\tilde{k}^4(\tilde{\omega}_1^2 + \tilde{\omega}_2^2)^2 - 4\tilde{k}^2(1 + \tilde{k}^2)\tilde{\omega}_1^2\tilde{\omega}_2^2\right)\gamma^2 + 2(\tilde{\omega}_1^2 + \tilde{\omega}_2^2)^2\tilde{k}^2\gamma + (\tilde{\omega}_1^2 + \tilde{\omega}_2^2)^2 - 4(1 + \tilde{k}^2)\tilde{\omega}_1^2\tilde{\omega}_2^2 = 0 \quad (59)$$

and its roots,

$$\begin{aligned} \gamma_{1,2} &= \frac{-(\tilde{\omega}_1^2 + \tilde{\omega}_2^2)^2\tilde{k}^2 \pm \sqrt{(\tilde{\omega}_1^2 + \tilde{\omega}_2^2)^4\tilde{k}^4 - \left(\tilde{k}^4(\tilde{\omega}_1^2 + \tilde{\omega}_2^2)^2 - 4\tilde{k}^2(1 + \tilde{k}^2)\tilde{\omega}_1^2\tilde{\omega}_2^2\right)\left((\tilde{\omega}_1^2 + \tilde{\omega}_2^2)^2 - 4(1 + \tilde{k}^2)\tilde{\omega}_1^2\tilde{\omega}_2^2\right)}}{\tilde{k}^4(\tilde{\omega}_1^2 + \tilde{\omega}_2^2)^2 - 4\tilde{k}^2(1 + \tilde{k}^2)\tilde{\omega}_1^2\tilde{\omega}_2^2} = \\ &= \frac{-(\tilde{\omega}_1^2 + \tilde{\omega}_2^2)^2\tilde{k} \pm 2(1 + \tilde{k}^2)\tilde{\omega}_1\tilde{\omega}_2(\tilde{\omega}_2^2 - \tilde{\omega}_1^2)}{\tilde{k}\left[\tilde{k}^2(\tilde{\omega}_1^2 + \tilde{\omega}_2^2)^2 - 4(1 + \tilde{k}^2)\tilde{\omega}_1^2\tilde{\omega}_2^2\right]} \end{aligned} \quad (60)$$

are always real. Let us order the roots such that $\gamma_1 \leq \gamma_2$. Exceptionally, it can happen that the coefficient at γ^2 in (59) vanishes, and then there is only one root,

$$\gamma_1 = \frac{4(1 + \tilde{k}^2)\tilde{\omega}_1^2\tilde{\omega}_2^2 - (\tilde{\omega}_1^2 + \tilde{\omega}_2^2)^2}{2(\tilde{\omega}_1^2 + \tilde{\omega}_2^2)^2\tilde{k}^2} \quad (61)$$

For further discussion, it turns out to be useful to formally set in this case $\gamma_2 = \infty$.

The admissible range of slopes γ for which the expression in (55) is real is $[\gamma_1, \gamma_2]$ if the coefficient at γ^2 in (59) is negative, and $[-\infty, \gamma_1] \cup [\gamma_2, \infty]$ if that coefficient is positive. In the exceptional case when the coefficient is zero, the admissible range is $[\gamma_1, \infty)$, where γ_1 is given by (61). In this case, we formally set $\gamma_2 = \infty$, so that we can use the same description $[\gamma_1, \gamma_2]$ as for a negative coefficient. The coefficient at γ^2 in (59) is positive if

$$|\tilde{\omega}_2^2 - \tilde{\omega}_1^2|\tilde{k} > 2\tilde{\omega}_1\tilde{\omega}_2 \quad (62)$$

Let \mathcal{K}_a be the set of wave numbers $\tilde{k} \in \mathbb{R}^+$ for which condition (62) is satisfied, and $\mathcal{K}_b = \mathbb{R}^+ \setminus \mathcal{K}_a$. The set of slopes γ that lead to a real value of the expression in (55) for all wave numbers \tilde{k} can formally be described as

$$\Gamma = \mathcal{I}_a \cap \mathcal{I}_b \quad (63)$$

where

$$\mathcal{I}_a = (-\infty, \inf_{\tilde{k} \in \mathcal{K}_a} \gamma_1] \cup [\sup_{\tilde{k} \in \mathcal{K}_a} \gamma_2, \infty) \quad (64)$$

$$\mathcal{I}_b = [\sup_{\tilde{k} \in \mathcal{K}_b} \gamma_1, \inf_{\tilde{k} \in \mathcal{K}_b} \gamma_2] \quad (65)$$

In most cases, the set Γ needs to be determined numerically. However, we can be sure that it is nonempty, because it always contains $\gamma = 1$.

3. Results and Discussion

3.1. Discrete chain of particles with alternating masses

3.1.1. Dispersion diagram

The enriched continuum model proposed in the previous section is now tuned up to reproduce the dispersion curves of the discrete chain of two alternating masses m and M connected by springs with stiffness K , shown in Figure 1. The particle spacing is denoted as a .

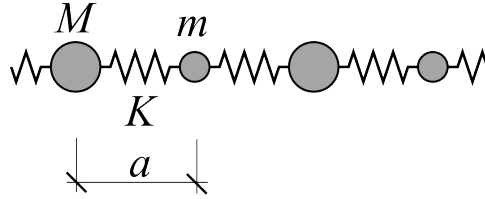


Figure 1: Schematic picture of a mass-spring chain with two alternating masses and only nearest-neighbor interactions

The dispersion relation of the considered discrete model is given by [42]

$$\omega_{1,2}^2 = \frac{K}{m} \left(1 + \beta \pm \sqrt{(1 + \beta)^2 - 4\beta \sin^2 ka} \right) = \frac{K}{m} \left(1 + \beta \pm \sqrt{1 + \beta^2 + 2\beta \cos 2ka} \right) \quad (66)$$

where $\beta = m/M$ is the ratio of the two masses. To fully specify the integral micromorphic model that has the same dispersion properties, we need to determine parameters ρ and η , and also weight functions E_0 , H_0 and A_0 . Recall that the integral of weight function E_0 over the whole real axis is the macroscopic modulus \bar{E} defined in (43).

Before we apply the developed procedure that provides Fourier images of the weight functions, it is necessary to convert the given dispersion diagram into the dimensionless form. The transformation is based on the choice of a characteristic length l and characteristic time τ , which should be related to the properties of the considered discrete model. The choice is not completely arbitrary, because the acoustic branch of the dimensionless dispersion diagram should have a unit slope at the origin. The acoustic branch ω_1 is obtained by using the negative sign in (66). For small wave numbers k , the formula can be approximated by

$$\omega_1^2 \approx \frac{K}{m} \left(1 + \beta - \sqrt{(1 + \beta)^2 - 4\beta k^2 a^2} \right) \approx \frac{K}{m} \left(1 + \beta - (1 + \beta) \left(1 - \frac{1}{2} \frac{4\beta}{(1 + \beta)^2} k^2 a^2 \right) \right) = \frac{K}{m} \frac{2\beta}{1 + \beta} k^2 a^2 \quad (67)$$

This indicates that

$$\frac{d\omega_1(0)}{dk} = \sqrt{\frac{2\beta K}{(1 + \beta)m}} a = \sqrt{\frac{2K}{M + m}} a \quad (68)$$

Since the scaling of the circular frequency by characteristic time τ and of the wave number by characteristic length l leads to $d\tilde{\omega}/d\tilde{k} = (\tau/l) d\omega/dk$, condition $d\tilde{\omega}(0)/d\tilde{k} = 1$ is satisfied if

$$\frac{l}{\tau} = \sqrt{\frac{2K}{M+m}} a \quad (69)$$

The ratio between scaling parameters l and τ is thus fixed, but one of these parameters can be freely selected and the other is then deduced from (69).

Since the length scale of the discrete model is controlled by the particle spacing a , one natural choice could be $l = a$, leading to $\tau = \sqrt{(M+m)/(2K)}$. However, nothing prevents us from setting $l = \lambda a$ where λ is a positive number. The corresponding characteristic time is then $\tau = \lambda \sqrt{(M+m)/(2K)}$ and the dimensionless dispersion relation is given by

$$\tilde{\omega}_{1,2}^2 = \lambda^2 \frac{1+\beta}{2\beta} \left(1 + \beta \pm \sqrt{(1+\beta)^2 - 4\beta \sin^2 \frac{\tilde{k}}{\lambda}} \right) \quad (70)$$

The dispersion diagrams are visualized in Figure 2 for various coefficients β and for $\lambda = 1$. It is sufficient to consider $\beta \in (0, 1]$ because the curves do not change if β is replaced by its reciprocal value, $1/\beta$. If λ is changed, the curves keep the same shape, only the scale on both axes is adjusted by the same factor.

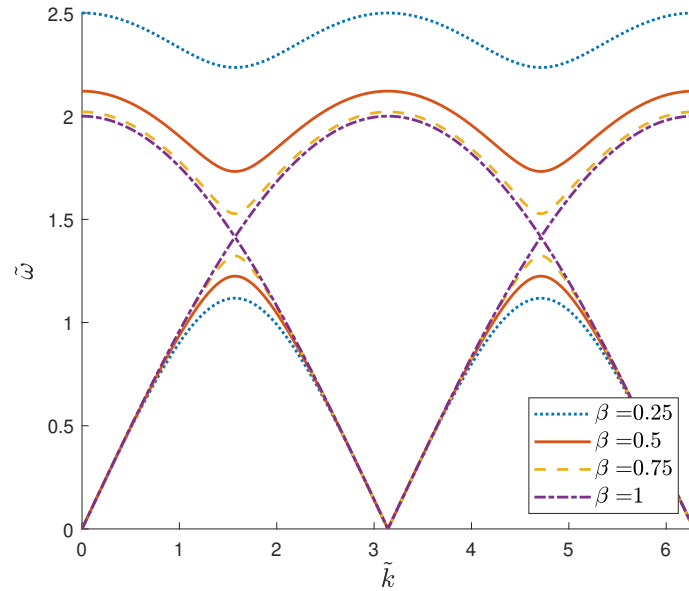


Figure 2: Dispersion diagram of the mass-spring chain with alternating masses, $\lambda = 1$

In the subsequent calculations, we focus on the case of $\beta = 0.5$, which means that $m = M/2$. Parameter λ is set to 1. The ellipses that are obtained by substituting (70) into (51) are plotted in Figure 3 for dimensionless wave numbers ranging between 1 and π .

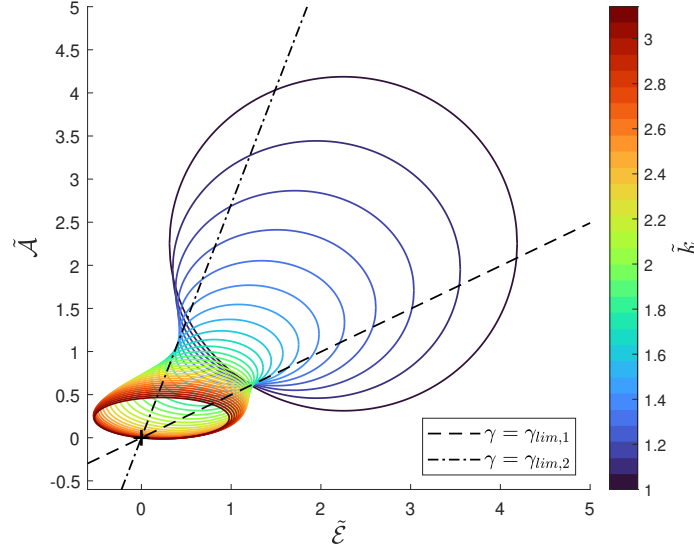


Figure 3: Solutions $\tilde{\mathcal{A}}$ and $\tilde{\mathcal{E}}$ visualized in the $\tilde{\mathcal{E}} - \tilde{\mathcal{A}}$ space for various wave numbers, with parameters $\beta = 0.5$ and $\lambda = 1$

3.1.2. Evaluation of Fourier images

Following the approach described in section 2.4 and assuming $\tilde{\mathcal{A}} = \gamma\tilde{\mathcal{E}}$, we express the solution according to formula (55) as

$$\tilde{\mathcal{E}} = \lambda^2 \frac{(1+\beta)^2}{2\beta(\gamma^2\tilde{k}^4 + \tilde{k}^2)} \left(\gamma\tilde{k}^2 + 1 - \sqrt{(\gamma\tilde{k}^2 + 1)^2 - 4(\gamma^2\tilde{k}^2 + 1)(1 + \tilde{k}^2)} \frac{\beta}{(1+\beta)^2} \sin^2 \frac{\tilde{k}}{\lambda} \right) \quad (71)$$

Thus, from a geometric point of view, the solution to Equation (51) is chosen as the intersection point of the ellipse and a straight line with slope γ passing through the origin (the intersection point closer to the origin is selected). To ensure that this line intersects the ellipse, and thus the solution is real, parameter γ needs to be chosen from the set Γ specified in (63). Substituting the given dispersion relations, formula (60) is rewritten as

$$\gamma_{1,2} = \frac{-(1+\beta)^2\tilde{k} \pm 2\sqrt{\beta} \sin \frac{\tilde{k}}{\lambda} (1 + \tilde{k}^2) \sqrt{\beta^2 + 2\beta \cos \frac{2\tilde{k}}{\lambda} + 1}}{\tilde{k}^3(1+\beta)^2 - 4\tilde{k}(1 + \tilde{k}^2)\beta \sin^2 \frac{\tilde{k}}{\lambda}} \quad (72)$$

For a given wave number \tilde{k} , lines with the slope γ_1 or γ_2 are tangent to the ellipse that depicts the set of possible solutions. The dependence of two roots on the wave number is visualized in Figure 4a, with the smaller root γ_1 plotted in blue and the larger root γ_2 plotted in red. The difference between the two sides of inequality (62) as a function of the wave number is shown in Figure 4b. As was discussed in Section 2.4, the sign of this expression determines the sign of the coefficient at γ^2 in Eq. (59) and hence the type of the interval for admissible γ coefficients. As seen in the graph, the sign is positive for $\tilde{k} \in \mathcal{K}_a = (0, \tilde{k}_1) \cup (\tilde{k}_2, \infty)$ and nonpositive for $\tilde{k} \in \mathcal{K}_b = [\tilde{k}_1, \tilde{k}_2]$, where $\tilde{k}_1 \approx 0.45$ and $\tilde{k}_2 \approx 1.92$. By applying the rules described in Section 2.4, it can be deduced from Figure 4a that the set of admissible γ parameters is $\Gamma = [\gamma_{lim,1}, \gamma_{lim,2}] \approx [0.4983, 2.7065]$, i.e., the interval between the dashed-dotted and dashed lines. From Figure 3, where the limiting slopes are also plotted by dashed lines, one can visually check that for $\gamma_{lim,1} < \gamma < \gamma_{lim,2}$ the straight lines with slope γ passing through the origin indeed intersect all the ellipses.

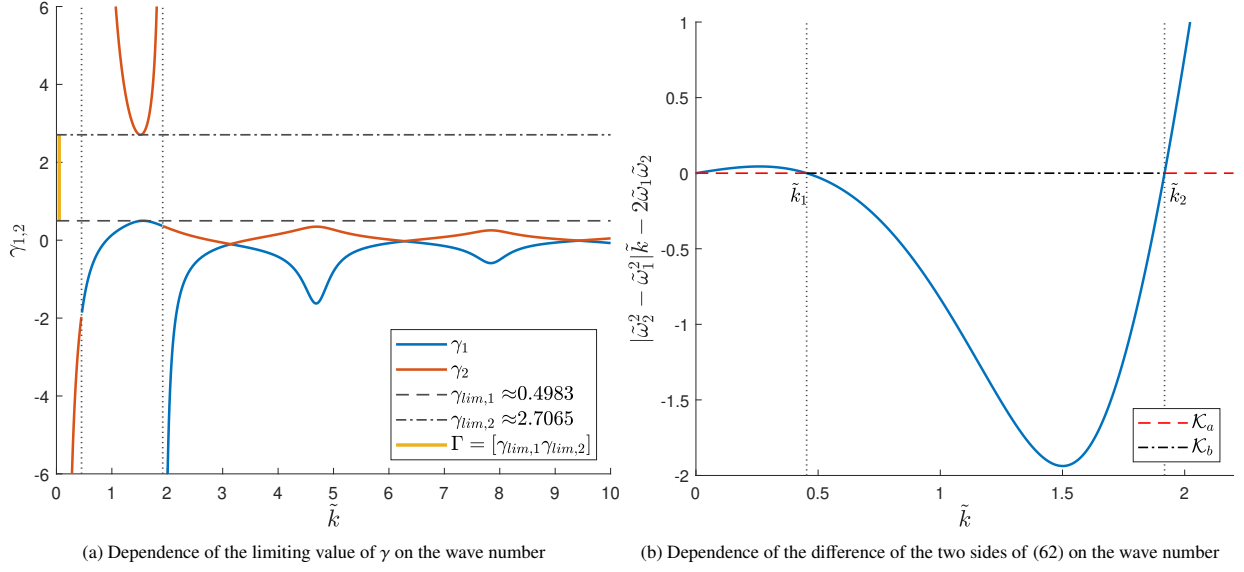


Figure 4: Graphical illustration of the admissible set Γ for parameters $\beta = 0.5$ and $\lambda = 1$

In Figure 5a, the Fourier images $\tilde{\mathcal{E}}(\tilde{k})$ calculated from (71) are plotted by solid lines for various choices of parameter γ . Function $\tilde{\mathcal{H}}$ is then obtained by substituting (70)–(71) into (56), which yields

$$\tilde{\mathcal{H}} = \tilde{\mathcal{H}}_a + \tilde{\mathcal{H}}_b + \tilde{\mathcal{H}}_c \quad (73)$$

where

$$\tilde{\mathcal{H}}_a = \lambda^2 \frac{(1 + \beta)^2}{\beta(1 + \tilde{k}^2)} \quad (74)$$

$$\tilde{\mathcal{H}}_b = -\lambda^2 \frac{(\gamma + 1)(1 + \beta)^2(\gamma\tilde{k}^2 + 1)}{2\beta(\gamma^2\tilde{k}^2 + 1)(1 + \tilde{k}^2)} \quad (75)$$

$$\tilde{\mathcal{H}}_c = \lambda^2 \frac{(1 + \beta)(\gamma + 1)}{2\beta} \frac{\sqrt{(1 + \beta)^2(\gamma\tilde{k}^2 + 1)^2 - 4(\gamma^2\tilde{k}^2 + 1)(1 + \tilde{k}^2)\beta \sin^2(\tilde{k}/\lambda)}}{(\gamma^2\tilde{k}^2 + 1)(1 + \tilde{k}^2)} \quad (76)$$

are three terms to be processed separately, as will be shown later. The graphs of $\tilde{\mathcal{H}}$ obtained for selected values of parameter γ are plotted by solid lines in Figure 5b. The value of $\tilde{\mathcal{H}}$ at $\tilde{k} = 0$ is $\tilde{\mathcal{H}}(0) = \lambda^2(1 + \beta)^2/\beta$, which indicates that the integral $\int_{\mathcal{L}} \tilde{H}(\tilde{r}) d\tilde{r}$ is finite.

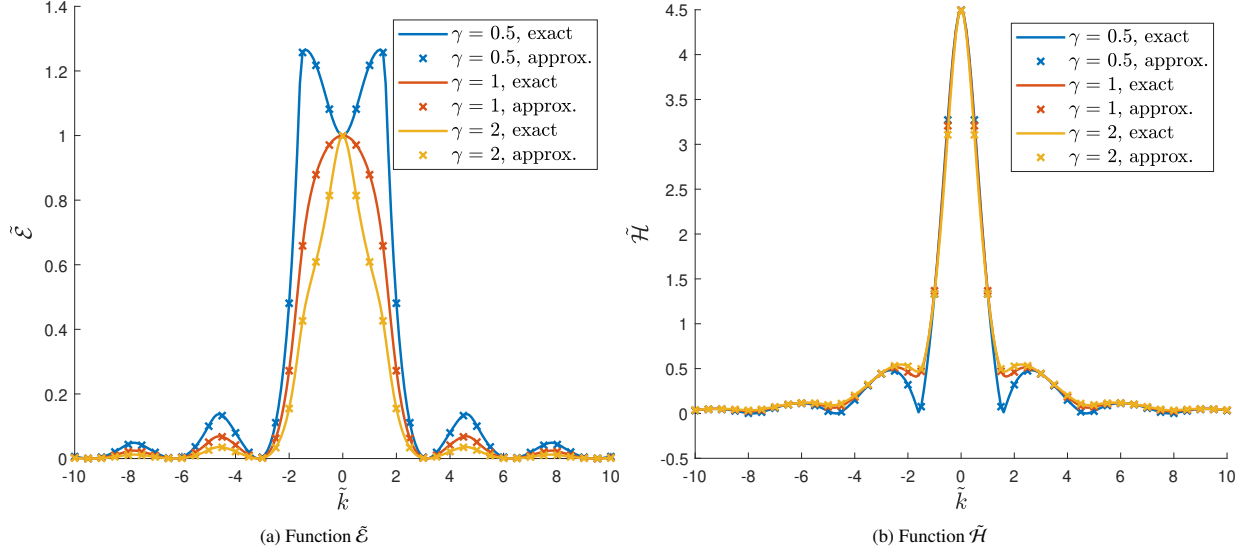


Figure 5: Fourier images of weight functions and their approximations evaluated for a double-mass-spring chain with $\beta = m/M = 0.5$ and $\lambda = 1$ (the cross symbols correspond to numerical evaluation according to (83) and their meaning will be described later)

The last weight function to be determined is $\tilde{\mathcal{A}} = \gamma\tilde{\mathcal{E}}$. Its graph is only a scaled graph of the already known function $\tilde{\mathcal{E}}$.

3.1.3. Reconstruction of the weight functions

So far, we have described the procedure leading to the Fourier images of the weight functions. To reconstruct the original weight functions \tilde{E} , \tilde{A} , and \tilde{H} in the space domain, the inverse Fourier transform (IFT) is applied to the already determined functions $\tilde{\mathcal{E}}$, $\tilde{\mathcal{A}}$, and $\tilde{\mathcal{H}}$. It is not always possible to perform the inverse transformation analytically; therefore, the inverse discrete Fourier transform (IDFT) is adopted in order to approximate the exact result. According to (73), the Fourier image $\tilde{\mathcal{H}}$ is composed of three parts, from which the first two, $\tilde{\mathcal{H}}_a$ and $\tilde{\mathcal{H}}_b$, can be transformed analytically, and only the third part $\tilde{\mathcal{H}}_c$ needs to be transformed numerically. The analytical inverse transforms read

$$\mathcal{F}^{-1}(\tilde{\mathcal{H}}_a) = \mathcal{F}^{-1}\left(\lambda^2 \frac{(1+\beta)^2}{\beta(1+\tilde{k}^2)}\right) = \lambda^2 \frac{(1+\beta)^2}{2\beta} e^{-|\tilde{r}|} \quad (77)$$

$$\mathcal{F}^{-1}(\tilde{\mathcal{H}}_b) = \mathcal{F}^{-1}\left(-\lambda^2 \frac{(\gamma+1)(1+\beta)^2(\gamma\tilde{k}^2+1)}{2\beta(\gamma^2\tilde{k}^2+1)(1+\tilde{k}^2)}\right) = -\lambda^2 \frac{(1+\beta)^2}{4\beta} (e^{-|\tilde{r}|} + e^{-|\tilde{r}|/\gamma}) \quad (78)$$

and the complete weight function is given by

$$\tilde{H} = \lambda^2 \frac{(1+\beta)^2}{4\beta} (e^{-|\tilde{r}|} - e^{-|\tilde{r}|/\gamma}) + \mathcal{F}^{-1}(\tilde{\mathcal{H}}_c) \quad (79)$$

Function $\tilde{\mathcal{E}}$ given by (71) can also be additively decomposed into two parts, the first of which could be transformed analytically. However, both parts have an infinite limit for $\tilde{k} \rightarrow 0$, which would result in numerical problems when solely the second part is transformed using the IDFT method. Therefore, the complete function $\tilde{\mathcal{E}}$ is transformed numerically.

The accuracy of the IDFT depends on the number of (positive) sampling points N in the wave number domain and on the length of the finite sampling interval, denoted by \tilde{k}_0 . The influence of both parameters on the resulting accuracy is now studied for the case when $\gamma = 0.5$. Figure 6 contains graphs of the approximated weight functions $\tilde{E}(\tilde{r})$ and $\tilde{H}(\tilde{r})$ computed for fixed $\tilde{k}_0 = 40$ and a varying number of sampling points. The sampling points are located at $\tilde{k}_j = j \Delta\tilde{k}$, $j = 0, 1, 2, \dots, N$, in which $\Delta\tilde{k} = \tilde{k}_0/N$ is the spacing (in the wave number domain).

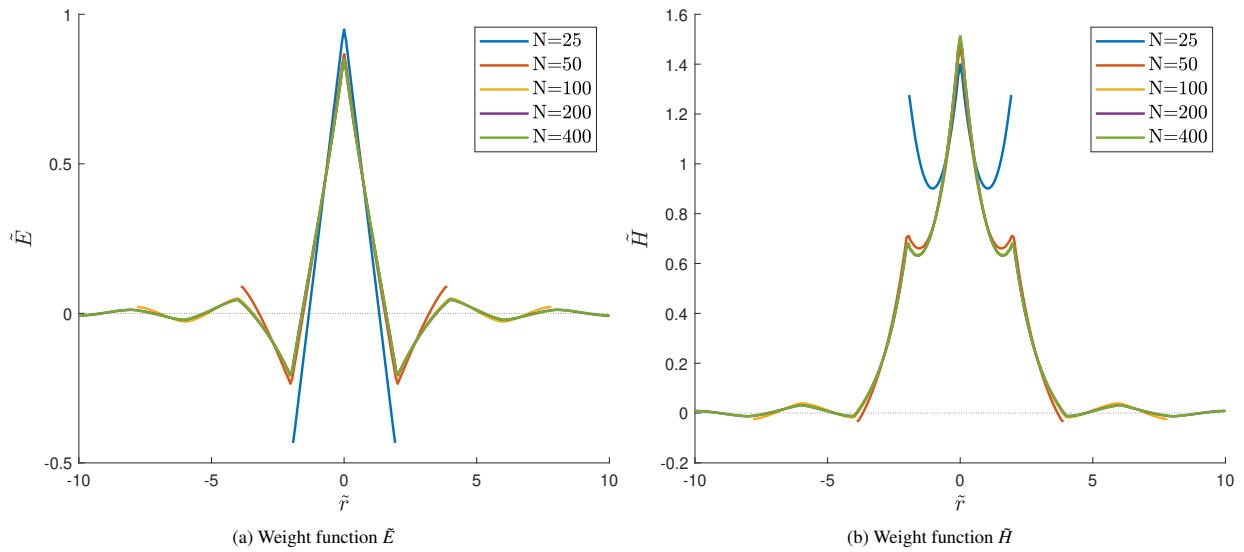


Figure 6: Weight functions computed by IDFT for the double-mass-spring chain for various numbers of positive sampling points N ; model parameters $\beta = 0.5$, $\gamma = 0.5$, $\lambda = 1$ and numerical parameter $\tilde{k}_0 = 40$

One can note that the shape of the weight functions seems to be stabilized for $N = 200$, since the result is visually indistinguishable from the result for $N = 400$. Subsequently, the effect of the sampling interval length is studied, with the number of sampling points set to $N = 400$. In Figure 7, the resulting graphs are displayed. It is apparent that, except for the blue line corresponding to $\tilde{k}_0 = 10$, all the other curves are almost identical.

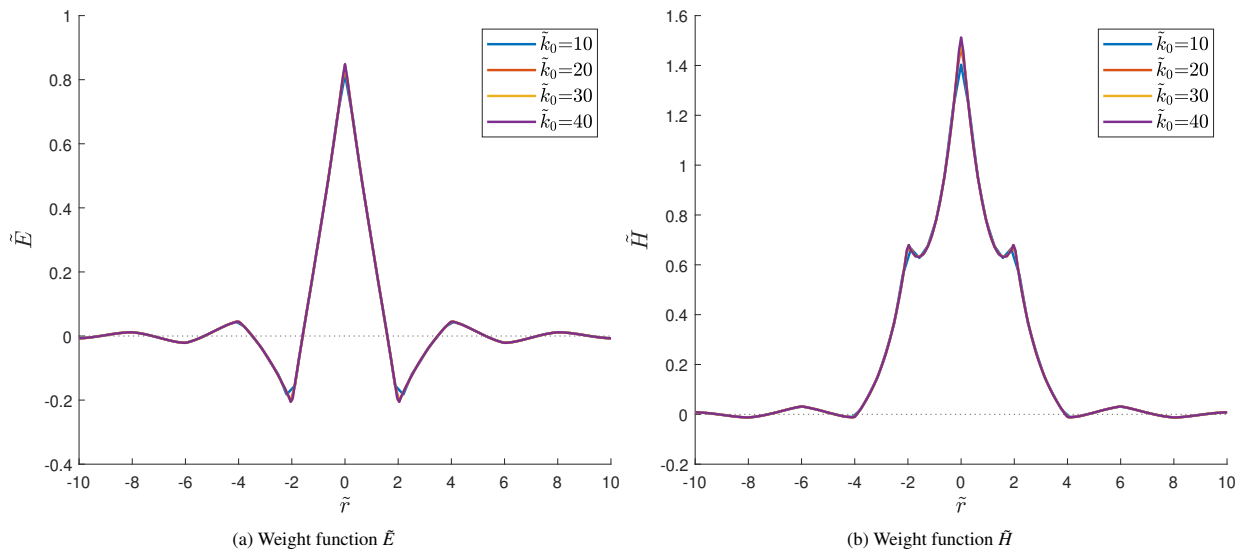


Figure 7: Weight functions computed by IDFT for the double-mass-spring chain for various lengths of the sampling interval k_0 ; model parameters $\beta = 0.5$, $\lambda = 1$, $\gamma = 0.5$ and numerical parameter $N = 400$

Overall, the numerically approximated results obtained with parameters $\tilde{k}_0 = 40$, and $N = 400$ are considered as sufficiently accurate and are adopted for further processing. Figure 8 shows the resulting approximations of the dimensionless weight functions evaluated for various coefficients γ .

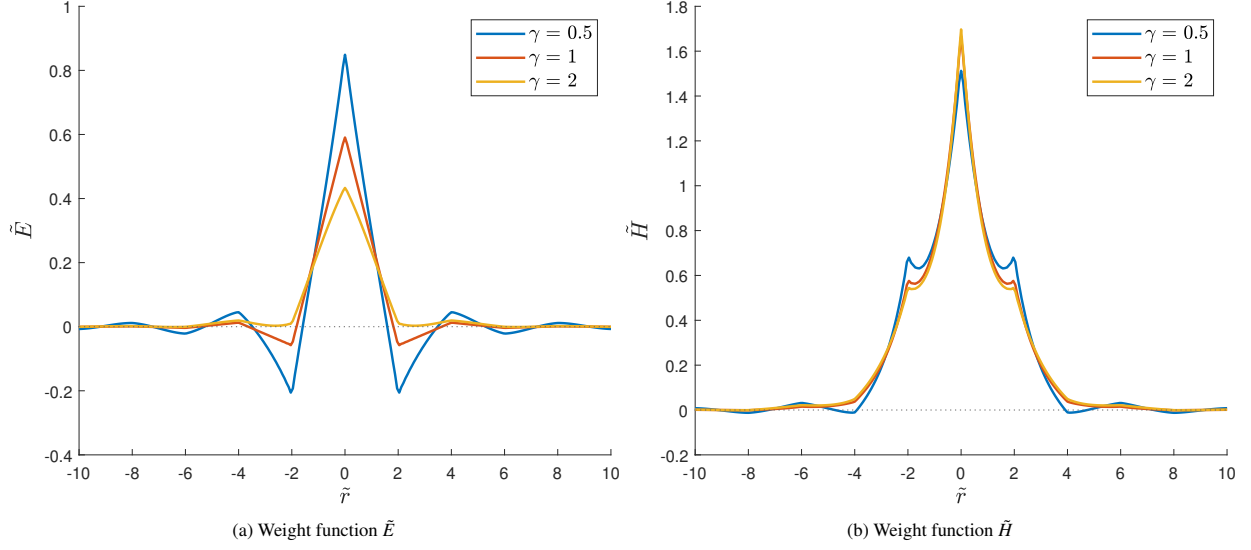


Figure 8: Weight functions computed by IDFT for the double-mass-spring chain; model parameters $\beta = 0.5$, $\lambda = 1$ and numerical parameters $\tilde{k}_0 = 40$, $N = 400$

The accuracy of the obtained pointwise approximations of weight functions \tilde{E} and \tilde{H} can be assessed by evaluating their Fourier images and comparing them to the analytical expressions in (71) and (73)–(76). By the IDFT one obtains approximate values of the weight function at non-negative positions $\tilde{r}_j = jh$ where $j = 0, 1, 2, \dots, N$ and $h = 2\pi N/\tilde{k}_0/(2N + 1)$ is the spacing in the dimensionless physical domain; these values can then be mirrored to the region of negative coordinates, since the weight functions are even. To approximate the dimensionless weight function, linear interpolation is used between neighboring positions \tilde{r}_j . The piecewise linear approximation can be expressed as

$$\tilde{E}(\tilde{r}) \approx \sum_{j=0}^N \tilde{E}_j \phi_j(\tilde{r}) + \sum_{j=1}^N \tilde{E}_j \phi_j(-\tilde{r}) \quad (80)$$

where \tilde{E}_j denotes the approximate value of the dimensionless weight function \tilde{E} at position \tilde{r}_j , and $\phi_j(\tilde{r})$ stands for the hat function defined as

$$\phi_j(\tilde{r}) = \begin{cases} 0 & \tilde{r} \in (-\infty, \tilde{r}_j - h) \\ \frac{\tilde{r} - (\tilde{r}_j - h)}{h} & \tilde{r} \in [\tilde{r}_j - h, \tilde{r}_j] \\ \frac{\tilde{r}_j + h - \tilde{r}}{h} & \tilde{r} \in [\tilde{r}_j, \tilde{r}_j + h] \\ 0 & \tilde{r} \in (\tilde{r}_j + h, \infty) \end{cases} \quad (81)$$

The Fourier transform of the hat function $\phi_j(\tilde{r})$ can be evaluated analytically and is given by

$$\Phi_j(\tilde{k}) = \int_{-\infty}^{\infty} \phi_j(\tilde{r}) \exp(-i\tilde{k}\tilde{r}) d\tilde{r} = h \left(\frac{\sin \frac{\tilde{k}h}{2}}{\frac{\tilde{k}h}{2}} \right)^2 \exp(-i\tilde{k}\tilde{r}_j) = \frac{4}{\tilde{k}^2 h} \sin^2 \frac{\tilde{k}h}{2} \exp(-i\tilde{k}\tilde{r}_j) \quad (82)$$

By virtue of the similarity theorem $\mathcal{F}(\phi_j(-\tilde{r})) = \Phi_j(-\tilde{k})$. Therefore, the Fourier transform of the approximated weight function is expressed as

$$\begin{aligned} \tilde{\mathcal{E}}(\tilde{k}) &\approx \sum_{j=0}^N \tilde{E}_j \Phi_j(\tilde{k}) + \sum_{j=1}^N \tilde{E}_j \Phi_j(-\tilde{k}) = \frac{4}{\tilde{k}^2 h} \sin^2 \frac{\tilde{k}h}{2} \left(\sum_{j=0}^N \tilde{E}_j \exp(-i\tilde{k}\tilde{r}_j) + \sum_{j=1}^N \tilde{E}_j \exp(i\tilde{k}\tilde{r}_j) \right) = \\ &= \frac{4}{\tilde{k}^2 h} \left(\tilde{E}_0 + 2 \sum_{j=1}^N \tilde{E}_j \cos \tilde{k}\tilde{r}_j \right) \sin^2 \frac{\tilde{k}h}{2} \end{aligned} \quad (83)$$

In the same spirit, also the approximation of function $\tilde{\mathcal{H}}(\tilde{k})$ can be constructed. In Figure 5, the obtained approximations of the Fourier images are visualized by star markers and compared to the exact functions. It is confirmed that the agreement is excellent.

Finally, one can assess the difference between the dispersion diagram of the double-mass-spring chain and the dispersion diagram of the enriched continuum model evaluated with the approximated weight functions that are plotted in Figure 8. The dispersion relation of the investigated continuum model is obtained by solving equation (28) for the unknown ω . In the dimensionless form and after substituting $\tilde{\mathcal{A}} = \gamma\tilde{\mathcal{E}}$, the solution reads

$$\tilde{\omega}_{1,2}^2 = \frac{\tilde{\mathcal{H}} + (\tilde{\mathcal{E}}(1 + \gamma) + \tilde{\mathcal{H}})\tilde{k}^2}{2} \pm \frac{\sqrt{(\tilde{\mathcal{H}} + (\tilde{\mathcal{E}}(1 + \gamma) + \tilde{\mathcal{H}})\tilde{k}^2)^2 - 4(\gamma\tilde{\mathcal{E}}(\tilde{\mathcal{E}} + \tilde{\mathcal{H}})\tilde{k}^4 + \tilde{\mathcal{E}}\tilde{\mathcal{H}}\tilde{k}^2)}}{2} \quad (84)$$

In Figure 9, the results obtained from (84) with the Fourier images $\tilde{\mathcal{E}}$ and $\tilde{\mathcal{H}}$ replaced by their approximations (83) are compared to the exact dispersion relation of the double-mass-spring chain given in (70). The dispersion diagrams are displayed in Figure 9a, and the difference between the exact and approximated results is visualized for the acoustic as well as optical branch in Figure 9b.

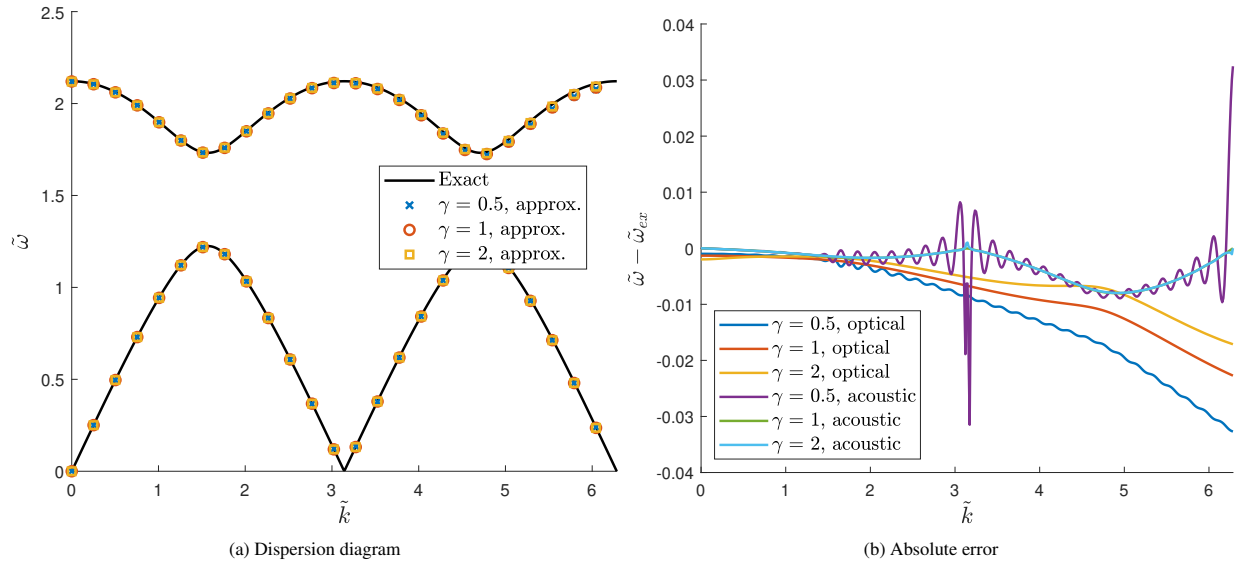


Figure 9: Comparison of the exact dispersion diagram of the double-mass-spring chain and its enriched continuum approximation for model parameters $\beta = 0.5$ and $\lambda = 1$ and numerical parameters $\tilde{k}_0 = 40$, $N = 400$

Figure 9b indicates that the error is greater for larger wave numbers. Moreover, the deviations are more severe for smaller parameters γ . From Figure 5a it is apparent that for decreasing parameter γ the amplitudes of the weight function get larger. Hence, a larger sampling window and a higher number of terms are required for the IDFT to achieve similar accuracy as for the function with larger values of γ .

3.1.4. Choice of characteristic length

So far, we have been working with a fixed value of $\lambda = 1$, meaning that the characteristic length of the continuum model is chosen equal to the particle spacing in the discrete chain. It is now interesting to look at the effect of parameter λ on the shape of the evaluated weight functions. Figure 10 shows the dimensionless Fourier images $\tilde{\mathcal{E}}$ and $\tilde{\mathcal{H}}$ obtained for a double-mass-spring chain with $\beta = 0.5$ using values of λ between 0.5 and 2. Parameter γ has a fixed value of 1, which means that functions $\tilde{\mathcal{E}}$ and $\tilde{\mathcal{A}}$ are identical. Function $\tilde{\mathcal{E}}$ is by definition normalized such that $\tilde{\mathcal{E}}(0) = 1$. For increasing λ , the graph of $\tilde{\mathcal{E}}$ is stretched horizontally, which corresponds to a change of scale. On the other hand, function $\tilde{\mathcal{H}}$ is not constrained by a normalizing condition, and its maximum increases with increasing λ , simultaneously with horizontal stretching and certain changes in shape.

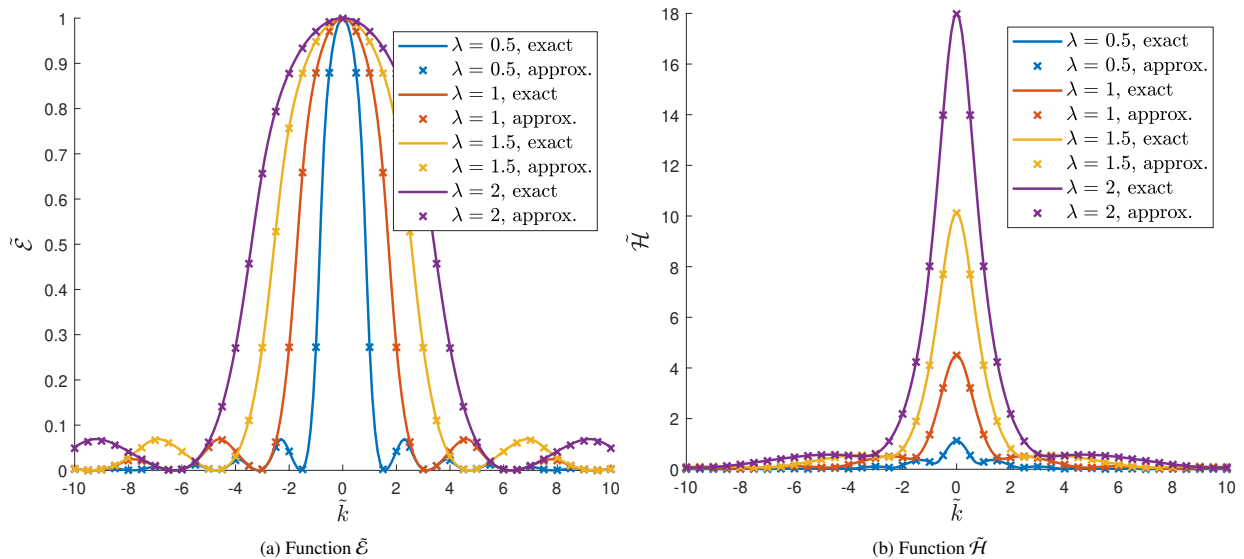


Figure 10: Fourier images of weight functions and their approximations evaluated for a double-mass-spring chain using fixed parameters $\beta = 0.5$ and $\gamma = 1$ and various values of λ

Dimensionless weight functions \tilde{E} and \tilde{H} obtained by inverse Fourier transformation are shown in Figure 11. For larger values of λ , function \tilde{E} is concentrated in a more narrow interval and its peak value is higher, while function \tilde{H} spreads over the same interval and its peak value is also higher. However, it is important to consider that the meaning of the dimensionless coordinate \tilde{r} depends on λ . The value of $\tilde{r} = 1$ corresponds to distance $r = l = \lambda a$ in the physical space. Moreover, when the dimensionless weight functions \tilde{E} and \tilde{H} are transformed into the physical ones, their values are multiplied by \tilde{E}/l , as follows from (44) and (46). Interestingly, the resulting weight function E_0 turns out to be independent of the choice of scaling factor λ , as shown in Figure 12a. This happens only in the particular case when $\gamma = 1$. Weight function E_0 constructed for instance for $\gamma = 2$ is already slightly affected by λ , as shown in Figure 12b. For the other weight functions, H_0 and A_0 , the effect of λ is always felt, even for $\gamma = 1$; see Figure 12c-f.

It is also interesting to observe that the weight functions, in particular the nonlocal elastic modulus E_0 and the nonlocal micromorphic modulus A_0 , strongly “feel” the interparticle spacing, a . The most important contribution to the corresponding nonlocal integrals comes from the neighborhood of radius $2a$. For the nonlocal coupling modulus, H_0 , the effective interaction distance increases with increasing λ , i.e., with increasing characteristic length l , but even this function has clearly marked kinks at distance $r = 2a$. This means that these functions reflect the discrete structure of the underlying mass-spring model, which is periodic and consists of repeated units of size $2a$.

When converting the nonlocal micromorphic model to a dimensionless format, the characteristic length was defined as $l = \sqrt{\eta/\rho}$, i.e., as a parameter related to the inertia effects. Alternatively, one could define a characteristic length related to stiffness, which would be

$$l_s = \sqrt{\frac{\bar{A}}{\bar{E}}} = \sqrt{\frac{\int_{-\infty}^{\infty} A_0(r) dr}{\int_{-\infty}^{\infty} E_0(r) dr}} \quad (85)$$

Exact matches of the same dispersion diagram of the spring-mass chain with alternating masses can be obtained with different combinations of length parameters l and l_s , but if one of them is selected, the other is determined uniquely. We have developed a procedure based on the selection of $l = \sqrt{\eta/\rho}$ as the primary independent parameter, along with equivalent modulus \bar{E} and characteristic time $\tau = \sqrt{\eta/\bar{E}}$. After conversion to the dimensionless form, we are able to determine dimensionless weight functions; their identification is unique only if additional assumptions are made—function \mathcal{A} is assumed to be a multiple of function \mathcal{E} with a fixed factor γ , and the ratio between the characteristic length l of the continuum model and characteristic length a of the discrete model is set to a given value λ . The obtained dimensionless functions can be transformed into their physical counterparts. To complete the identification

process, it is necessary to express the basic parameters of the continuum model in terms of the four basic parameters of the discrete model from Fig. 1, namely a , m , M , and K . The relations that have already been established, i.e., $l = \lambda a$ and $\tau = \lambda \sqrt{(M + m)/(2K)}$, can be rewritten in terms of the original parameters as

$$\frac{\eta}{\rho} = \lambda^2 a^2 \quad (86)$$

$$\frac{\eta}{\bar{E}} = \lambda^2 \frac{M + m}{2K} \quad (87)$$

Note that λ is not a true parameter of the discrete model—along with γ it is one of two parameters that can be chosen more or less arbitrarily (within certain limits). Therefore, the parameters of the continuum and discrete models must satisfy only one constraint,

$$\frac{\bar{E}}{\rho} = \frac{2Ka^2}{M + m} \quad (88)$$

If the only objective was to capture the given dispersion diagram, we could select one of parameters \bar{E} and ρ arbitrarily and then evaluate the other one from the above condition. Physically, this means that we would only need to make sure that the long-wave limit of the elastic wave speed is the same for both models. However, it makes good sense to add a simple condition that will endow ρ with the physical meaning of macroscopic density, and then \bar{E} will automatically get the meaning of macroscopic elastic modulus that links, under homogeneous deformation, strain to stress. The added condition can be based on the matching of kinetic energy that corresponds to the motion of the whole bar or chain as a rigid body at constant speed v . For the micromorphic continuum model, this motion is characterized by $u(x, t) = u_0 + vt$ and $\chi(x, t) = 0$, and the corresponding kinetic energy density (per unit volume) is $\rho v^2/2$. For the discrete model with alternating masses m and M at distance a , the kinetic energy per unit length would be $(M + m)v^2/(4a)$. To be able to compare these expressions, we would need to define the area of the continuous bar that represents the mass-spring chain. However, this would be just an additional factor for conversion between 3D and 1D, which does not need to be introduced if we consider masses M and m as taken per unit area (of the equivalent continuous bar) and also stiffness K as the actual spring stiffness divided by the area. The fractions on the right-hand sides of (87) and (88) then remain the same while the kinetic energy $(M + m)v^2/(4a)$ is taken per unit volume and thus can be directly set equal to $\rho v^2/2$. The resulting condition

$$\rho = \frac{M + m}{2a} \quad (89)$$

naturally reflects the fact that the equivalent density of the continuous bar is obtained by uniform smearing of the concentrated masses along the bar. When this is substituted into (88), we obtain

$$\bar{E} = Ka \quad (90)$$

as the expression for equivalent macroscopic modulus of the continuum model. In this way, parameters \bar{E} and ρ , which would be preserved by the standard continuum theory without any micromorphic or nonlocal enhancements, can be directly deduced from the properties of the mass-spring chain. Of course, the standard continuum model is non-dispersive and provides only a linear acoustic branch of the dispersion diagram.

The non-standard parameter η related to micromorphic inertia can be expressed according to (86) as

$$\eta = \lambda^2 a^2 \rho = \lambda^2 a \frac{M + m}{2} \quad (91)$$

However, λ is a chosen parameter, independent of the given characteristics of the mass-spring chain, and so η is in fact arbitrary and λ is just a conveniently transformed dimensionless value that can be used for comparison of the characteristic length induced by the choice of η with the spacing between masses in the discrete model.

Once \bar{E} and ρ have been set to values that reflect the properties of the mass-spring chain and dimensionless parameters λ (as a transformed version of the micromorphic inertia parameter η) and γ have been selected (within reasonable bounds), the procedure described above leads to certain uniquely defined nonlocal weight functions E_0 ,

A_0 , and H_0 . It is then meaningful to characterize the relative “strength” of individual nonlocal effects by the ratios between the integrals of the weight functions over the whole real axis. In fact, the ratio

$$\frac{\int_{-\infty}^{\infty} A_0(r) dr}{\int_{-\infty}^{\infty} E_0(r) dr} = \frac{\bar{A}}{\bar{E}} = l_s^2 \quad (92)$$

is the square of the alternative (stiffness-related) characteristic length l_s , which was introduced in (85). Functions E_0 and H_0 have the same physical dimension, and so the fraction

$$\frac{\int_{-\infty}^{\infty} H_0(r) dr}{\int_{-\infty}^{\infty} E_0(r) dr} = \frac{\bar{H}}{\bar{E}} = \kappa \quad (93)$$

is dimensionless and measures the ratio between the coupling micromorphic stiffness and the standard stiffness.

Making use of our previous results and assumptions, we can express

$$\bar{H} = \int_{-\infty}^{\infty} H_0(r) dr = \frac{\bar{E}}{l} \int_{-\infty}^{\infty} \tilde{H}_0(\tilde{r}) l d\tilde{r} = \bar{E} \tilde{\mathcal{H}}(0) \quad (94)$$

$$\bar{A} = \int_{-\infty}^{\infty} A_0(r) dr = \bar{E} l \int_{-\infty}^{\infty} \tilde{A}_0(\tilde{r}) l d\tilde{r} = \bar{E} l^2 \tilde{\mathcal{A}}(0) = \bar{E} l^2 \gamma \quad (95)$$

from which

$$l_s^2 = \frac{\bar{A}}{\bar{E}} = l^2 \gamma \quad (96)$$

$$\kappa = \frac{\bar{H}}{\bar{E}} = \tilde{\mathcal{H}}(0) = \tilde{\omega}_2^2(0) = \tau^2 \omega_2^2(0) = \frac{\eta \omega_2^2(0)}{\bar{E}} \quad (97)$$

Relation (96) means that, by choosing parameter γ , we set the ratio between the squares of characteristic lengths l_s and l , which are related to micromorphic stiffness and micromorphic inertia, respectively. From this point of view, it makes sense that γ needs to be taken from a certain interval which always contains value 1. For $\gamma = 1$, both characteristic lengths coincide. Relation (97) links the ratio κ to parameters η and \bar{E} and to the circular frequency at the starting point of the optical branch. For the considered discrete model, this frequency is $\omega_2(0) = \sqrt{2K(M+m)/(mM)}$, and we get

$$\kappa = \frac{2K(M+m)}{mM} \lambda^2 \frac{M+m}{2K} = \lambda^2 \frac{(M+m)^2}{mM} \quad (98)$$

The fraction that involves M and m depends on the discrete model, but parameter λ is determined by our choice of the characteristic length related to micromorphic inertia. When more weight is given to micromorphic inertia effects, then the area under the weight function that couples the micromorphic strain to the standard strain must also be increased, in proportion to the square of the characteristic length.

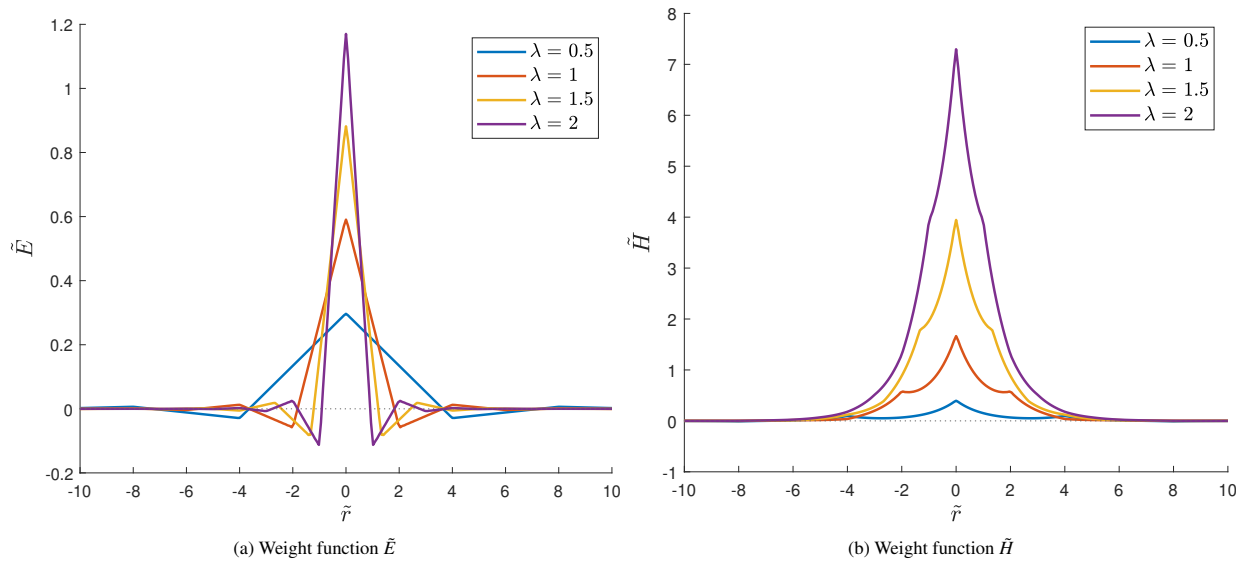


Figure 11: Weight functions computed by IDFT for the double-mass-spring chain using fixed parameters $\beta = 0.5$ and $\gamma = 1$ and various values of λ

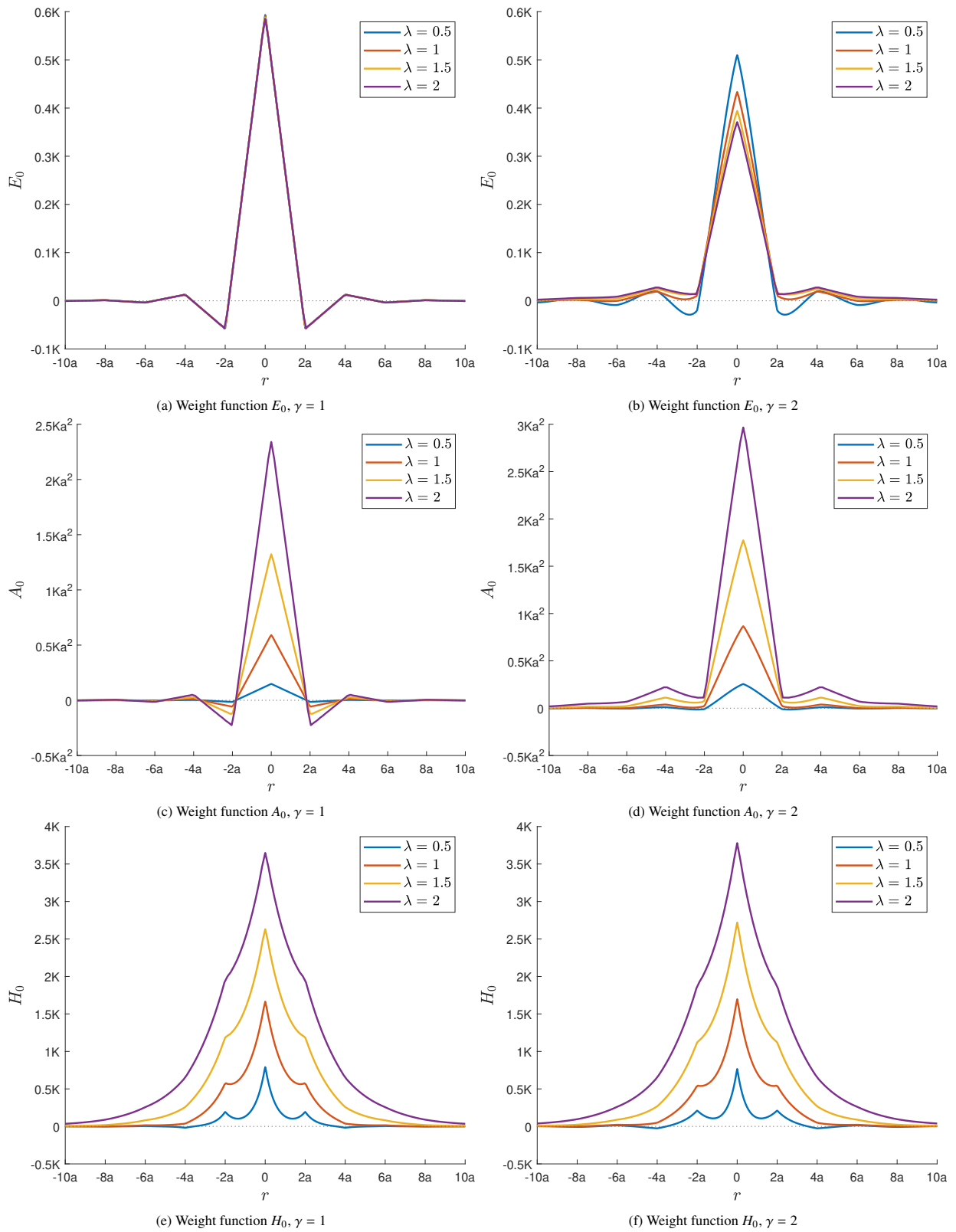


Figure 12: Physical (not dimensionless) weight functions evaluated for the double-mass-spring chain using various values of λ , two representative values of γ , and fixed $\beta = 0.5$

3.2. Remarks on the complexity of the model

The approach used so far has been based on the assumption that weight function \tilde{A} is a multiple of weight function \tilde{E} . It has been shown that, with a suitable choice of the proportionality factor, this constraint leads to a unique solution for all three weight functions involved. It is now logical to ask whether the class of considered formulations could not be restricted in another way, e.g., by reducing the general nonlocality imposed on all three terms of the free energy (10) to a formulation for which one of the terms remains local. This is formally equivalent to replacing one of the general weight functions by a multiple of the Dirac delta distribution, and the Fourier transform of such a weight function is a constant function for every wave number \tilde{k} .

Based on Figure 3 it is possible to explain why neither $\tilde{A}(\tilde{r})$ nor $\tilde{E}(\tilde{r})$ can be chosen as a multiple of the Dirac distribution. Each individual ellipse depicts the set of all admissible solutions for a fixed wave number. A constant Fourier image $\tilde{\mathcal{A}}$ (or $\tilde{\mathcal{E}}$) would correspond to finding one fixed vertical (or horizontal) line that intersects the ellipses constructed for all wave numbers \tilde{k} , which is not possible. The reason is that as the wave number increases, the corresponding ellipse shrinks and its center approaches the origin in the $(\tilde{\mathcal{E}}, \tilde{\mathcal{A}})$ plane. The projection of the ellipse on the vertical axis is a finite interval $[\tilde{\mathcal{A}}_{min}, \tilde{\mathcal{A}}_{max}]$, and from the description of the ellipse by equation (51) it follows that

$$\tilde{\mathcal{A}}_{max} = \frac{(\tilde{\omega}_1^2 + \tilde{\omega}_2^2)\tilde{k} + |\tilde{\omega}_2^2 - \tilde{\omega}_1^2| \sqrt{\tilde{k}^2 + 1}}{2\tilde{k}^3} \quad (99)$$

This upper limit depends on the wave number \tilde{k} not only explicitly, but also through the circular frequencies $\tilde{\omega}_{1,2}$. Substituting the specific expressions (70) that describe the dimensionless dispersion diagram of the double-mass-spring model, we obtain

$$\tilde{\mathcal{A}}_{max}(\tilde{k}) = \frac{\lambda^2(1+\beta)^2}{2\beta\tilde{k}^3} \left(\tilde{k} + \sqrt{(\tilde{k}^2 + 1) \left(1 - \frac{4\beta}{(1+\beta)^2} \sin^2 \frac{\tilde{k}}{\lambda} \right)} \right) \leq \frac{\lambda^2(1+\beta)^2}{2\beta} \cdot \frac{\tilde{k} + \sqrt{\tilde{k}^2 + 1}}{\tilde{k}^3} \quad (100)$$

where λ and β are given positive parameters (notice that $4\beta/(1+\beta)^2 \leq 1$). Based on the inequality in (100), it is easy to prove that $\lim_{\tilde{k} \rightarrow \infty} \tilde{\mathcal{A}}_{max}(\tilde{k}) = 0$. Therefore, for any fixed $\tilde{\mathcal{A}}^* > 0$, there exist certain wave numbers \tilde{k} for which $\tilde{\mathcal{A}}_{max}(\tilde{k}) < \tilde{\mathcal{A}}^*$ and thus the horizontal straight line at $\tilde{\mathcal{A}} = \tilde{\mathcal{A}}^*$ does not intersect the corresponding ellipses. Consequently, the dispersion relation cannot be satisfied for all wave numbers if the weight function \tilde{A} is a multiple of the Dirac distribution.

In a very similar way, it is possible to show that the upper limit

$$\tilde{\mathcal{E}}_{max}(\tilde{k}) = \frac{\lambda^2(1+\beta)^2}{2\beta\tilde{k}^2} \left(1 + \sqrt{(\tilde{k}^2 + 1) \left(1 - \frac{4\beta}{(1+\beta)^2} \sin^2 \frac{\tilde{k}}{\lambda} \right)} \right) \leq \frac{\lambda^2(1+\beta)^2}{2\beta} \cdot \frac{1 + \sqrt{\tilde{k}^2 + 1}}{\tilde{k}^2} \quad (101)$$

of the interval $[\tilde{\mathcal{E}}_{min}, \tilde{\mathcal{E}}_{max}]$ that represents the projection of the ellipse on the horizontal axis also tends to zero as the wave number tends to infinity, and so it is not possible to choose a fixed positive value $\tilde{\mathcal{E}}^*$ of Fourier image $\tilde{\mathcal{E}}$ and obtain a real solution $\tilde{\mathcal{A}}$ of equation (50) for all wave numbers. In fact, the only candidate would be $\tilde{\mathcal{E}}^* = 1$ because the adopted conversion to the dimensionless formulation always yields $\tilde{\mathcal{E}}(0) = 1$, but this does not invalidate the reasoning.

So far, it has been demonstrated that the terms with weight functions E_0 and A_0 must remain truly nonlocal (i.e., regular weight functions need to be used). The last case to be explored is what happens if function $\tilde{H}(\tilde{r})$ is chosen as a multiple of the Dirac distribution, leading to a constant Fourier image $\tilde{\mathcal{H}}(\tilde{k})$. In view of (97), the constant value would correspond to the previously introduced parameter $\kappa = \tilde{H}/\tilde{E}$. In our general framework, $\tilde{\mathcal{H}}$ is linked to the other Fourier images $\tilde{\mathcal{E}}$ and $\tilde{\mathcal{A}}$ by relation (52), and so the assumption that $\tilde{\mathcal{H}}(\tilde{k}) = \kappa$ leads to

$$\frac{\tilde{\omega}_1^2 + \tilde{\omega}_2^2 - (\tilde{\mathcal{A}} + \tilde{\mathcal{E}})\tilde{k}^2}{1 + \tilde{k}^2} = \kappa \quad (102)$$

Using this constraint, $\tilde{\mathcal{A}}$ can be expressed as

$$\tilde{\mathcal{A}} = \frac{\tilde{\omega}_1^2 + \tilde{\omega}_2^2 - (1 + \tilde{k}^2)\kappa}{\tilde{k}^2} - \tilde{\mathcal{E}} \quad (103)$$

and eliminated from (50), which leads to a quadratic equation for $\tilde{\mathcal{E}}$ with a discriminant given by

$$D = \tilde{k}^4 \left((\tilde{\omega}_2^2 - \tilde{\omega}_1^2)^2 - 4\tilde{k}^2 \kappa^2 \right) \quad (104)$$

To obtain a real Fourier image $\tilde{\mathcal{E}}$, we would need $D \geq 0$ for all $\tilde{k} \geq 0$. For $\kappa > 0$, this would be possible only if $\tilde{\omega}_2^2 - \tilde{\omega}_1^2 = O(\tilde{k})$ as $\tilde{k} \rightarrow \infty$. Some dispersion diagrams may satisfy such a condition, but if both branches are bounded, the condition is violated and the only possibility would be to set κ to zero, which leads to a model with no coupling between the displacement and the micromorphic strain. For instance, for the double-mass-spring chain, the dimensionless dispersion relation (70) implies that

$$\tilde{\omega}_2^2 - \tilde{\omega}_1^2 = \lambda^2 \frac{1+\beta}{\beta} \sqrt{(1+\beta)^2 - 4\beta \sin^2 \frac{\tilde{k}}{\lambda}} \leq \lambda^2 \frac{(1+\beta)^2}{\beta} \quad (105)$$

and the discriminant becomes negative for sufficiently large wave numbers (of course, unless $\kappa = 0$).

In summary, in this subsection it has been shown that nonlocality is needed in all three terms of the free energy function in order to reproduce the dispersion diagram of the double-mass-spring chain.

3.3. Mass-spring chain with equal masses

In this section, we investigate how the weight functions look when the masses in the double-mass-spring chain are equal, i.e., when $\beta = m/M = 1$. For such a simple mass-spring chain, the dispersion diagram has only one (acoustic) branch. However, substituting $\beta = 1$ into equation (70) that describes the double-mass chain, we obtain

$$\tilde{\omega}_{1,2}^2 = 2\lambda^2 \left(1 \pm \cos \frac{\tilde{k}}{\lambda} \right) = \begin{cases} 4\lambda^2 \cos^2 \frac{\tilde{k}}{2\lambda} \\ 4\lambda^2 \sin^2 \frac{\tilde{k}}{2\lambda} \end{cases} \quad (106)$$

The corresponding dispersion diagram is visualized by the dash-dotted line in Figure 2. Note that two branches still exist, since the two masses are treated separately.

The branches obtained for $\beta = 1$ intersect at those wave numbers \tilde{k} for which $\cos(\tilde{k}/\lambda) = 0$. This has important consequences. If $\tilde{\omega}_1 = \tilde{\omega}_2$ for some \tilde{k} , the ellipse described by (51) reduces to a single point with coordinates $\tilde{\mathcal{E}} = \tilde{\mathcal{A}} = \tilde{\omega}_1^2/\tilde{k}^2$, and it is intersected only by one line passing through the origin—the one with the unit slope. Therefore, $\gamma = 1$ is the only possible choice for this model. Furthermore, when \tilde{k} passes through one of the points at which $\cos(\tilde{k}/\lambda) = 0$, the expression under the square root in (54) becomes zero and it is possible, for the subsequent interval until the next $\cos(\tilde{k}/\lambda) = 0$, to revert the sign before the square root without losing continuity. As a result, the expression for the Fourier image $\tilde{\mathcal{E}}$ based on formula (71) can be written as

$$\tilde{\mathcal{E}} = \frac{2\lambda^2}{\tilde{k}^2} \left(1 - \cos \frac{\tilde{k}}{\lambda} \right) \quad (107)$$

without the need to replace the cosine term with its absolute value. The inverse Fourier transform of such a function can be evaluated analytically, leading to

$$\tilde{E}(\tilde{r}) = \lambda \max(1 - \lambda|\tilde{r}|, 0) = \lambda \langle 1 - \lambda|\tilde{r}| \rangle \quad (108)$$

where the Macauley brackets $\langle \dots \rangle$ denote the positive part. Since $\gamma = 1$, we have $\tilde{\mathcal{A}} = \tilde{\mathcal{E}}$ and $\tilde{A} = \tilde{E}$. After transformation into the physical space based on scaling relations (44)–(45), the weight functions are given by

$$E_0(r) = \frac{\tilde{E}}{l} \tilde{E} \left(\frac{r}{l} \right) = \frac{\tilde{E}}{l} \lambda \left\langle 1 - \frac{\lambda|r|}{l} \right\rangle = \frac{\tilde{E}}{a} \left\langle 1 - \frac{|r|}{a} \right\rangle \quad (109)$$

$$A_0(r) = \tilde{E} l \tilde{A} \left(\frac{r}{l} \right) = \tilde{E} l \lambda \left\langle 1 - \frac{\lambda|r|}{l} \right\rangle = l^2 \frac{\tilde{E}}{a} \left\langle 1 - \frac{|r|}{a} \right\rangle \quad (110)$$

Here we have exploited the relation $\lambda = l/a$ to express the final results in terms of the particle spacing a and characteristic length l . It is remarkable that weight function E_0 depends only on the physical parameters, \bar{E} and a , and is independent of the choice of l . The second weight function, A_0 , is simply E_0 multiplied by the square of the selected characteristic length, which can be arbitrarily adjusted.

The Fourier image $\tilde{\mathcal{H}}$ of the third weight function is in the present case given by

$$\tilde{\mathcal{H}} = \frac{4\lambda^2}{1 + \tilde{k}^2} \cos \frac{\tilde{k}}{\lambda} \quad (111)$$

and the corresponding dimensionless weight function obtained analytically by the inverse Fourier transform has the form

$$\tilde{H}(\tilde{r}) = \lambda^2 \left(e^{-|\tilde{r}|/\lambda + \tilde{r}} + e^{-|\tilde{r}|/\lambda - \tilde{r}} \right) \quad (112)$$

from which

$$H_0(r) = \frac{\bar{E}}{l} \tilde{H}\left(\frac{r}{l}\right) = \frac{\bar{E}}{l} \lambda^2 \left(e^{-|\lambda+r/l|} + e^{-|\lambda-r/l|} \right) = \frac{\bar{E}l}{a^2} \left(e^{-|r+a/l|} + e^{-|r-a/l|} \right) \quad (113)$$

The model with the derived weight functions E_0 , A_0 , and H_0 should always give the same dispersion diagram, independently of the choice of parameter l . As $l \rightarrow 0^+$, functions A_0 and H_0 tend to zero functions and the model reduces to a simpler nonlocal strain model, with no micromorphic terms. This is consistent with the results described in [15], where the dispersion diagram of a simple mass-spring chain was shown to be exactly reproduced by a nonlocal strain model with weight function (109).

Recall that, according to (91), the micromorphic inertia η is proportional to $\lambda^2 a$ and therefore to l^2 (for fixed physical parameters a , m , and M that characterize the mass-spring chain). In the limit, when $l = 0$, the micromorphic inertia vanishes and the micromorphic strain field does not affect the kinetic or potential energy. The optical branch of the dispersion diagram then totally vanishes. Since η was used in the definitions of the characteristic time and characteristic length, this case needs to be analyzed separately, starting again from the dispersion equation (28). For $\eta = 0$, this equation simplifies to

$$-\rho(\mathcal{A}k^2 + \mathcal{H})\omega^2 + \mathcal{A}(\mathcal{E} + \mathcal{H})k^4 + \mathcal{E}\mathcal{H}k^2 = 0 \quad (114)$$

which is a single equation for three unknown functions \mathcal{E} , \mathcal{A} , and \mathcal{H} . Let us now substitute the dispersion relation for a single mass-spring chain, given by

$$\omega^2 = \frac{4K}{m} \sin^2 \frac{ak}{2} \quad (115)$$

and exploit (114) to express

$$\mathcal{E} = \frac{\rho\omega^2(\mathcal{H} + \mathcal{A}k^2) - \mathcal{A}\mathcal{H}k^4}{\mathcal{H}k^2 + \mathcal{A}k^4} = \frac{4\rho K}{mk^2} \sin^2 \frac{ak}{2} - \frac{\mathcal{A}\mathcal{H}k^2}{\mathcal{H} + \mathcal{A}k^2} \quad (116)$$

In the special case of vanishing \mathcal{A} , which corresponds to the standard integral continuum (non-micromorphic), the previous equation reduces to

$$\mathcal{E} = \frac{4\rho K}{mk^2} \sin^2 \frac{ak}{2} = \frac{2\rho K}{mk^2} (1 - \cos ak) \quad (117)$$

which is the same function as was derived in (107) for the case of nonvanishing microinertia, just not normalized.

3.4. Mass-spring chain with alternating masses and second-nearest-neighbor interactions

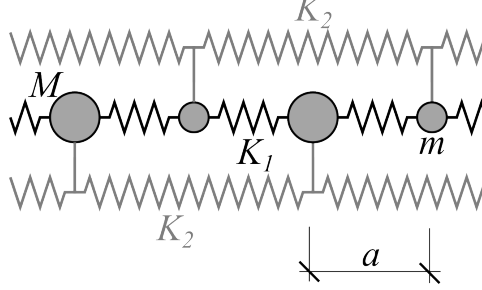


Figure 13: Mass-spring chain with two alternating masses

A slightly more complex dispersion diagram can be obtained by adding second-nearest-neighbor interactions to the double-mass-spring chain; see Figure 13. By a specific combination of the mass and stiffness parameters, the initial curvature of the dispersion diagram can be changed to positive, while without the long-range interaction, it is always negative. Let us denote the displacement of the larger mass M at position $x = 2na$ by u_{2n} and the displacement of the smaller mass m at the neighbouring position $x = (2n + 1)a$ by v_{2n+1} , and let K_1 be the stiffness of the springs connecting the nearest neighbors and K_2 the stiffness of the springs between the second-nearest neighbors. The equations of motion then read

$$M\ddot{u}_{2n} = K_1(v_{2n+1} - 2u_{2n} + v_{2n-1}) + K_2(u_{2n+2} - 2u_{2n} + u_{2n-2}) \quad (118)$$

$$m\ddot{v}_{2n+1} = K_1(u_{2n+2} - 2v_{2n+1} + u_{2n}) + K_2(v_{2n+3} - 2v_{2n+1} + v_{2n-1}) \quad (119)$$

Substituting the harmonic ansatz

$$u_{2n}(t) = U e^{i(2nka - \omega t)} \quad (120)$$

$$v_{2n+1}(t) = V e^{i((2n+1)ka - \omega t)} \quad (121)$$

we obtain the system of equations

$$\begin{aligned} -M\omega^2 U &= K_1(V(e^{ika} + e^{-ika}) - 2U) + K_2(U(e^{2ika} + e^{-2ika}) - 2U) \\ -m\omega^2 V &= K_1(U(e^{ika} + e^{-ika}) - 2V) + K_2(V(e^{2ika} + e^{-2ika}) - 2V) \end{aligned}$$

which has a nontrivial solution only if

$$\det \begin{pmatrix} -M\omega^2 + 2K_1 + 4K_2 \sin^2 ka & -2K_1 \cos ka \\ -2K_1 \cos ka & -m\omega^2 + 2K_1 + 4K_2 \sin^2 ka \end{pmatrix} = 0 \quad (122)$$

Solving this characteristic equation, we get the dispersion relation

$$\omega_{1,2}^2 = \frac{K_1}{m} \left((1 + \beta)(1 + 2\xi \sin^2 ka) \pm \sqrt{(1 + \beta)^2(1 + 2\xi \sin^2 ka)^2 - 4\beta(4\xi^2 \sin^2 ka + 4\xi + 1) \sin^2 ka} \right) \quad (123)$$

in which $\xi = K_2/K_1$ is the stiffness ratio.

Same as in the case of the original discrete model, transformation to the dimensionless form should be done such that the slope of the acoustic branch at the origin equals 1. Therefore, one needs to evaluate

$$\frac{d\omega_1(0)}{dk} = \sqrt{\frac{2\beta K_1(1 + 4\xi)}{(1 + \beta)m}} a = \sqrt{\frac{2(K_1 + 4K_2)}{M + m}} a \quad (124)$$

and then select the normalizing parameters l and τ such that their ratio meets the condition

$$\frac{l}{\tau} = \sqrt{\frac{2\beta K_1(1+4\xi)}{(1+\beta)m}} a = \sqrt{\frac{2(K_1+4K_2)}{M+m}} a \quad (125)$$

which guarantees that $d\tilde{\omega}(0)/d\tilde{k} = 1$. For instance, one can set the characteristic length l to a given multiple of the distance between the masses, i.e., $l = \lambda a$, and determine the characteristic time τ from (125). The resulting dimensionless form of (123) reads

$$\tilde{\omega}_{1,2}^2 = \lambda^2 \frac{1+\beta}{2\beta(1+4\xi)} \left((1+\beta) \left(1 + 2\xi \sin^2 \frac{\tilde{k}}{\lambda} \right) \pm \sqrt{(1+\beta)^2 \left(1 + 2\xi \sin^2 \frac{\tilde{k}}{\lambda} \right)^2 - 4\beta \left(4\xi^2 \sin^2 \frac{\tilde{k}}{\lambda} + 4\xi + 1 \right) \sin^2 \frac{\tilde{k}}{\lambda}} \right) \quad (126)$$

Adopting the same procedure as described in Section 3.1 for the chain with only nearest-neighbor interactions, we can construct an enriched continuum model that exactly reproduces the dispersion relation. In Figure 14, the numerically evaluated dimensionless weight functions obtained for parameters $\xi = K_2/K_1 = 0.4$ and $\beta = m/M = 0.5$ are displayed. The IDFT of the Fourier images of weight functions has been performed with numerical parameters $\tilde{k}_0 = 40$ and $N = 400$. To ensure that function $\tilde{\mathcal{E}}$ is real for every wave number \tilde{k} , parameter γ must be selected from $[0.4984, 2.6042]$. Interestingly, for $\gamma = 1$, the resulting weight function E_0 scaled into the physical space does not depend on parameter λ that sets the characteristic length for conversion into the dimensionless format. The length scale is dictated directly by the particle spacing a ; see Figure 15a. Weight function A_0 has the same support and shape for different values of λ , but its magnitude is affected by the choice of λ ; see Figure 15c. For other choices of γ , slightly different weight functions are obtained but their overall look remains similar. The agreement between the original dispersion diagram of the discrete model and its replica based on the continuum model is excellent for all parameter choices, as shown in Figure 16.

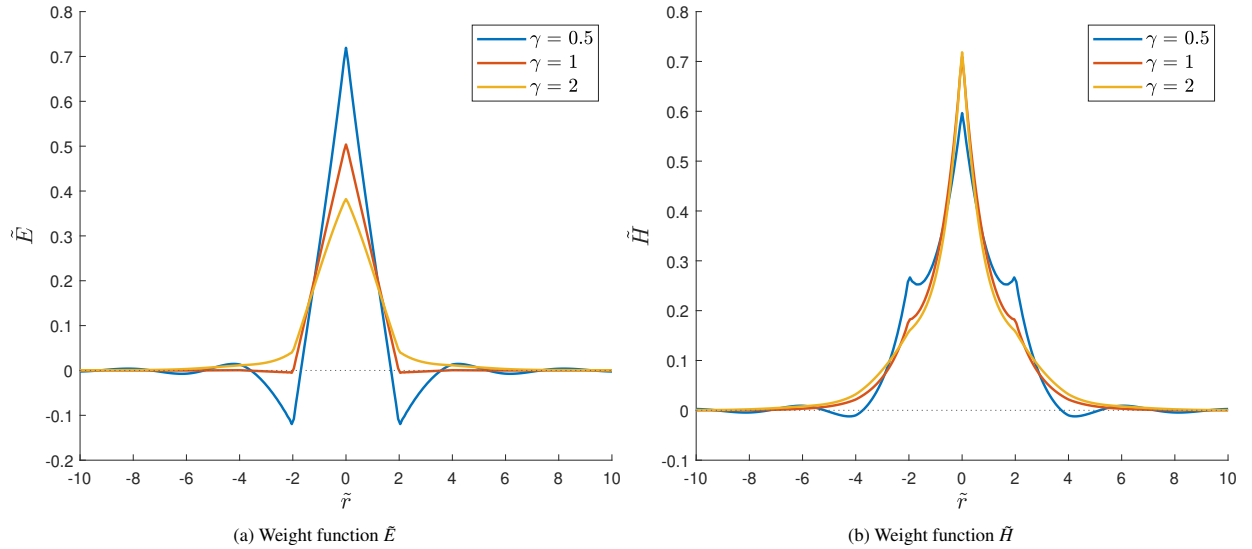


Figure 14: Weight functions computed by IDFT for the double-mass-spring chain with second-neighbour interactions, using model parameters $\beta = 0.5$, $\xi = 0.4$ and $\lambda = 1$ and numerical parameters $\tilde{k}_0 = 40$ and $N = 400$

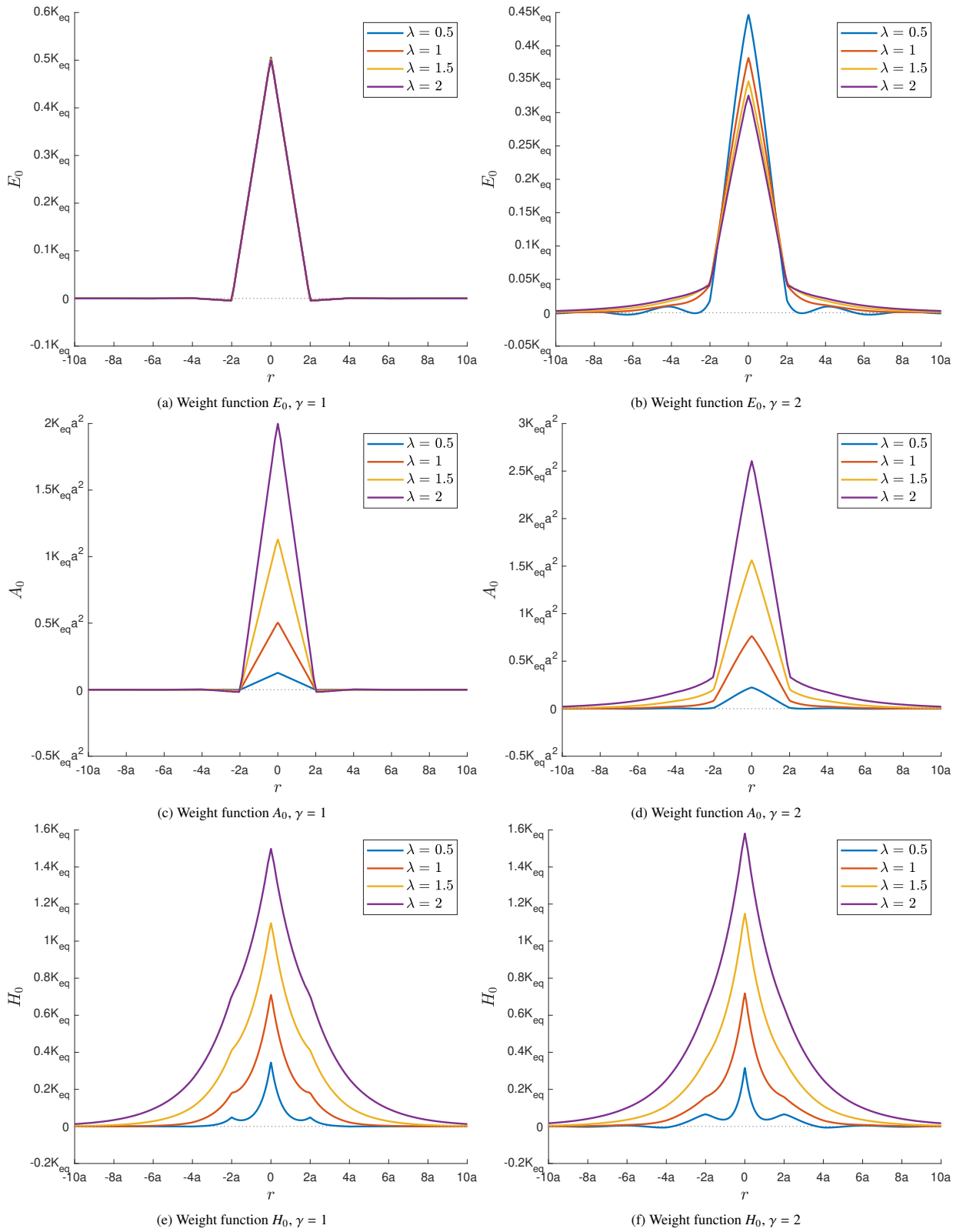


Figure 15: Weight functions (in physical space) evaluated for the double-mass-spring chain with second-nearest-neighbor interactions using various values of parameter λ and two different values of parameter γ , with fixed $K_{eq} = K_1 + 4K_2$, $\beta = 0.5$ and $\xi = 0.4$

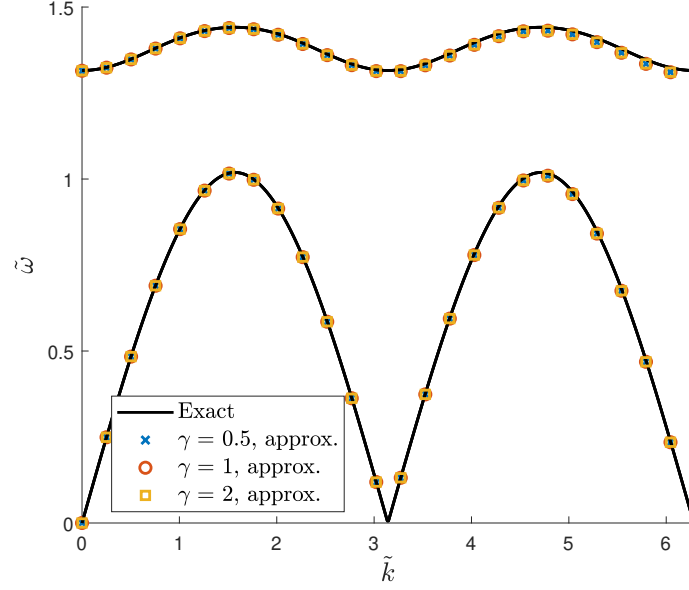


Figure 16: Comparison of the original dispersion diagram of the double-mass-spring chain with second-neighbor interactions and its replica based on the enriched continuum formulation with parameters $\beta = 0.5$, $\xi = 0.4$ and $\lambda = 1$

3.5. Reconstruction of the dispersion diagram with band gap obtained for local micromorphic model with vanishing micromorphic modulus

In [35] it was shown that, in the case of the 1D local micromorphic model, a band gap in the dispersion diagram can only be obtained when the micromorphic modulus (in [35] denoted by A) is set to zero. The dispersion relation then reads

$$\omega_{1,2}^2 = \frac{k^2(\bar{E} + \bar{H})\eta + \bar{H}\rho}{2\rho\eta} \pm \frac{\sqrt{(k^2(\bar{E} + \bar{H})\eta - \bar{H}\rho)^2 + 4k^2\bar{H}^2\rho\eta}}{2\rho\eta} \quad (127)$$

Normalizing the frequency and the wave number as described in section 2.3 and introducing parameter $\kappa = \bar{H}/\bar{E}$, we can rewrite equation (127) as

$$\tilde{\omega}_{1,2}^2 = \frac{\tilde{k}^2(1 + \kappa) + \kappa}{2} \pm \frac{\sqrt{(\tilde{k}^2(1 + \kappa) - \kappa)^2 + 4\tilde{k}^2\kappa^2}}{2} \quad (128)$$

from which

$$\tilde{\omega}_1^2 + \tilde{\omega}_2^2 = \tilde{k}^2(1 + \kappa) + \kappa \quad (129)$$

$$\tilde{\omega}_1^2\tilde{\omega}_2^2 = \tilde{k}^2\kappa \quad (130)$$

In this section, we show how the present nonlocal micromorphic model approximates such dispersion relations.

Since the local micromorphic formulation is a special case of the model introduced in this paper, one possible choice is to set $\tilde{E}(\tilde{r}) = \sqrt{\eta/\rho}\delta(\tilde{r})$, $\tilde{A}(\tilde{r}) = 0$, and $\tilde{H}(\tilde{r}) = \kappa\sqrt{\eta/\rho}\delta(\tilde{r})$, where $\delta(\tilde{r})$ denotes the Dirac delta distribution. The corresponding Fourier images are $\tilde{E}(\tilde{k}) = 1$, $\tilde{A}(\tilde{k}) = 0$, and $\tilde{H}(\tilde{k}) = \kappa$, and one can indeed check that equation (50) is satisfied when relations (129)–(130) are substituted. However, there exist infinitely many other combinations of weight functions for which the dispersion diagram is exactly reproduced. This can be demonstrated by plotting the set of all admissible solutions described by (51) with the squares of dimensionless circular frequencies substituted from (128). The corresponding graphs are displayed in Figure 17.

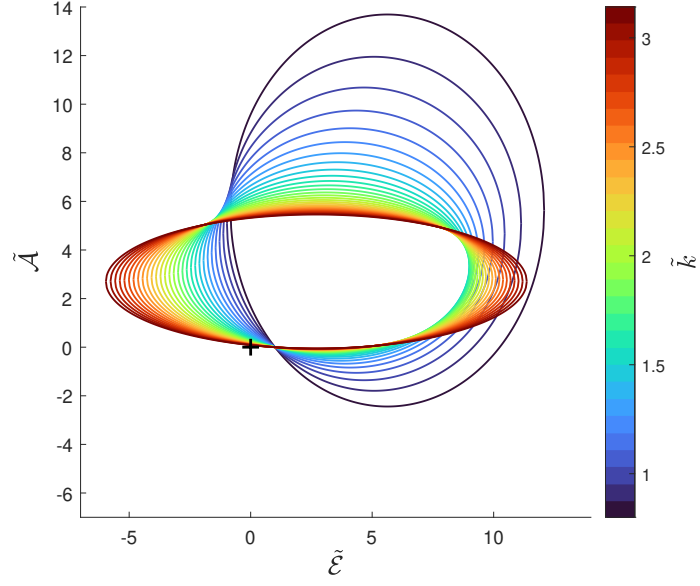


Figure 17: Solutions $\tilde{\mathcal{A}}$ and $\tilde{\mathcal{E}}$ visualized in the $\tilde{\mathcal{E}} - \tilde{\mathcal{A}}$ space for various wave numbers, $\kappa = 4$

One can now clearly see that all the ellipses pass through the point where $\tilde{\mathcal{E}}(\tilde{k}) = 1$ and $\tilde{\mathcal{A}}(\tilde{k}) = 0$, which corresponds to the local micromorphic model described above. Other possible models can be constructed by adopting the procedure described in section 2.4. Substituting (129) and (130) into (55) and (56), we express the dimensionless Fourier images as

$$\tilde{\mathcal{E}} = \frac{(\tilde{k}^2(1 + \kappa) + \kappa)(\gamma\tilde{k}^2 + 1) - \sqrt{(\tilde{k}^2(1 + \kappa) + \kappa)^2(\gamma\tilde{k}^2 + 1)^2 - 4(\gamma^2\tilde{k}^2 + 1)(1 + \tilde{k}^2)\tilde{k}^2\kappa}}{2(\gamma^2\tilde{k}^4 + \tilde{k}^2)} \quad (131)$$

$$\tilde{\mathcal{H}} = \kappa + \frac{\tilde{k}^2}{1 + \tilde{k}^2} - (1 + \gamma)\frac{\tilde{k}^2}{1 + \tilde{k}^2}\tilde{\mathcal{E}} \quad (132)$$

Parameter $\gamma = \tilde{\mathcal{A}}/\tilde{\mathcal{E}}$ can have an arbitrary positive value, since the expression in (131) is real for any $\gamma > 0$. In Figure 18, the graphs of Fourier images $\tilde{\mathcal{E}}$ and $\tilde{\mathcal{H}}$ are plotted for $\kappa = 4$ and for values of γ ranging from 0.5 to 4.

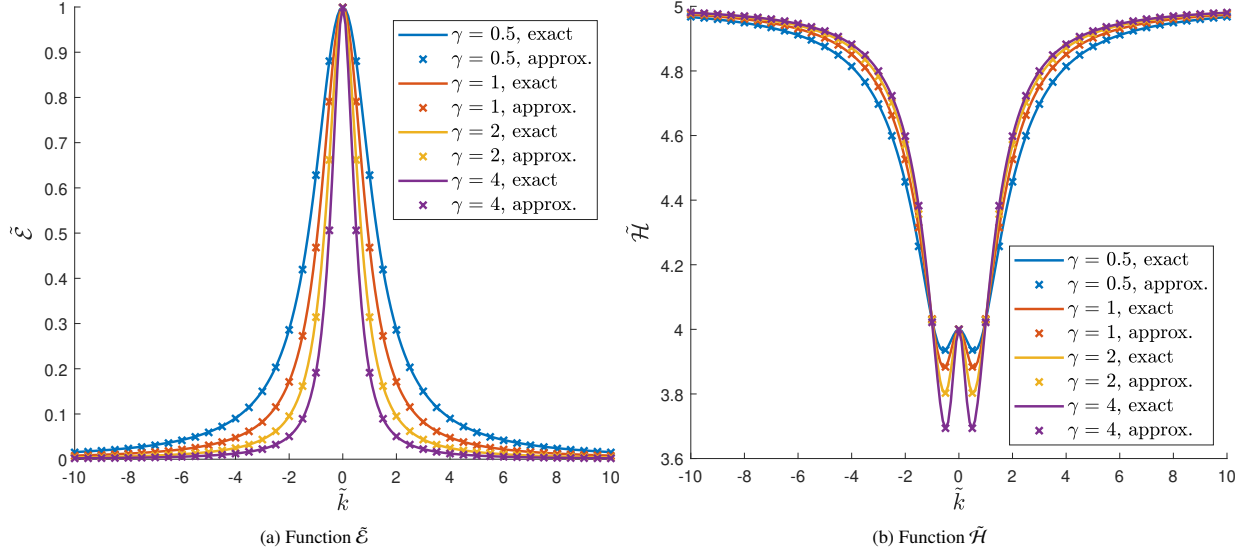


Figure 18: Comparison of the Fourier images of dimensionless weight functions and their approximation for $\kappa = 4$ and for various values of γ

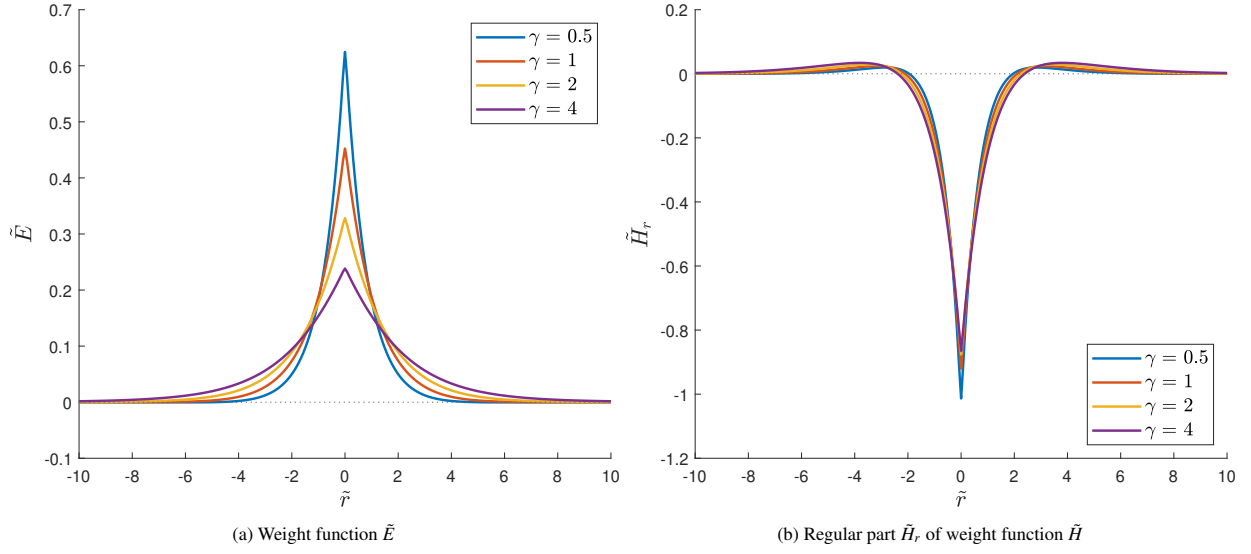


Figure 19: Weight functions computed by IDFT for the approximation of the dispersion diagram obtained from the local micromorphic model with vanishing micromorphic modulus, using various values of γ and fixed values of model parameter $\kappa = 4$ and numerical parameters $\tilde{k}_0 = 40$ and $N = 400$

It is interesting to note that, in the limit of $\tilde{k} \rightarrow \infty$, the value of $\tilde{\mathcal{E}}$ tends to zero but $\tilde{\mathcal{H}}$ approaches (from below) a positive limit $\kappa + 1$. This is caused by the first two terms in (132). Their inverse Fourier transform can be evaluated analytically and contains a multiple of the Dirac distribution:

$$\mathcal{F}^{-1}\left(\kappa + \frac{\tilde{k}^2}{1 + \tilde{k}^2}\right) = (1 + \kappa)\delta(\tilde{r}) - \frac{1}{2}e^{-|\tilde{r}|} \quad (133)$$

Therefore, the resulting weight function

$$\tilde{H} = \mathcal{F}^{-1}(\tilde{\mathcal{H}}) = \tilde{H}_s + \tilde{H}_r \quad (134)$$

consists of a singular part

$$\tilde{H}_s = (1 + \kappa) \delta(\tilde{r}) \quad (135)$$

and a regular part

$$\tilde{H}_r = -\frac{1}{2}e^{-|\tilde{r}|} - (1 + \gamma) \mathcal{F}^{-1} \left(\frac{\tilde{k}^2}{1 + \tilde{k}^2} \tilde{\mathcal{E}} \right) \quad (136)$$

The regular part, evaluated numerically, is plotted in Figure 19b, along with the full weight function \tilde{E} plotted in Figure 19a.

Finally, Figure 20 shows an excellent agreement between the dispersion diagram of the original local micromorphic model with $A = 0$, given by (128), and the dispersion diagram obtained using the present integral micromorphic model with various values of γ and with the corresponding weight functions \tilde{E} , \tilde{H} and \tilde{A} obtained by inverse Fourier transform of the functions in (131)–(132) and by setting $\tilde{A} = \gamma \tilde{E}$.

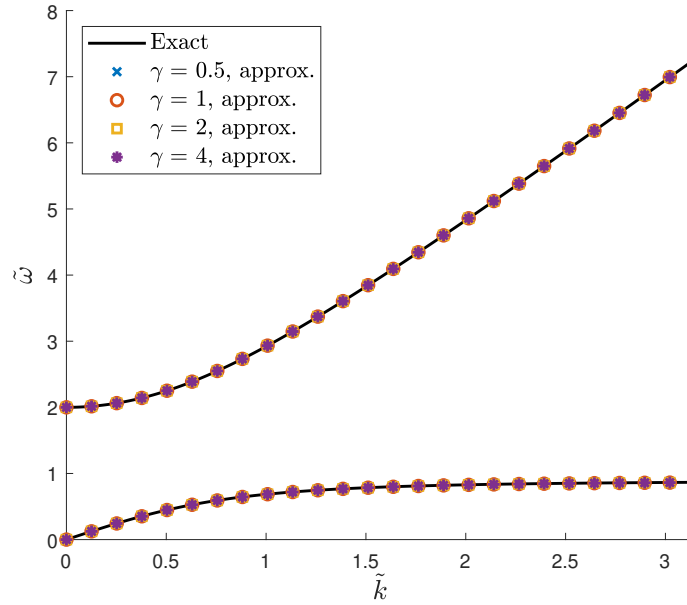


Figure 20: Comparison of the original dispersion diagram obtained from the local micromorphic model with vanishing micromorphic modulus and its replica obtained using the integral micromorphic model, with fixed $\kappa = 4$ and various values of γ

4. Energetic Aspects

4.1. General considerations

Since the proposed generalized continuum model has been consistently derived from expressions for the kinetic and potential energy, it is interesting to look at the relative contribution of individual terms in those expressions.

For a harmonic wave characterized by a certain wave number k and the corresponding circular frequency ω (linked to k by the dispersion equation (28)), the matrix in (23) is singular and, assuming that $\mathcal{H}_1 = \mathcal{H}_2 = \mathcal{H}$, we can express the ratio of the complex amplitudes

$$\frac{\hat{\chi}}{\hat{u}} = \frac{\rho\omega^2 - (\mathcal{E} + \mathcal{H})k^2}{\mathcal{H}ik} = \frac{(\mathcal{E} + \mathcal{H})k^2 - \rho\omega^2}{\mathcal{H}k} i = X i \quad (137)$$

where

$$X = \frac{(\mathcal{E} + \mathcal{H})k^2 - \rho\omega^2}{\mathcal{H}k} = \frac{\mathcal{H}k}{\mathcal{H} + \mathcal{A}k^2 - \eta\omega^2} \quad (138)$$

is real. This indicates that the phase shift between the micromorphic variable and the displacement field is always either $\pi/2$, or $-\pi/2$ (depending on the sign of X). Consequently, if the real representation of the displacement field is given by

$$u(x, t) = \hat{u} \cos(kx - \omega t) \quad (139)$$

where \hat{u} is real, then the micromorphic strain field is described by

$$\chi(x, t) = -X\hat{u} \sin(kx - \omega t) \quad (140)$$

Based on this, it is possible to evaluate the corresponding kinetic and potential energy associated with the harmonic elastic wave.

In an infinite body, the energy would also be infinite, but it makes sense to determine its (uniform) spatial average, which remains finite. For a harmonic wave, it is sufficient to average over one wave length. According to (11), the spatially averaged kinetic energy is expressed as

$$\begin{aligned} \bar{T} &= \frac{k}{2\pi} \int_0^{\frac{2\pi}{k}} \left(\frac{1}{2} \rho \dot{u}(x, t)^2 + \frac{1}{2} \eta \dot{\chi}(x, t)^2 \right) dx = \\ &= \frac{k}{4\pi} \rho \omega^2 \hat{u}^2 \int_0^{\frac{2\pi}{k}} \sin^2(kx - \omega t) dx + \frac{k}{4\pi} \eta \omega^2 X^2 \hat{u}^2 \int_0^{\frac{2\pi}{k}} \cos^2(kx - \omega t) dx = \frac{1}{4} (\rho + \eta X^2) \omega^2 \hat{u}^2 \end{aligned} \quad (141)$$

The result is independent of time, even though we have applied averaging in space only. The reason is that the considered wave travels through the infinite space without changing its form and the distribution of velocities at two time instants is only shifted in space.

Evaluation of the potential energy is more tedious because it requires double integration. The local strain is given by

$$u'(x, t) = -k\hat{u} \sin(kx - \omega t) \quad (142)$$

and thus it is useful to prepare the weighted spatial average

$$\begin{aligned} \int_{\mathcal{L}} E_0(x - \xi) \sin(k\xi - \omega t) d\xi &= \int_{\mathcal{L}} E_0(r) \sin(kx - kr - \omega t) dr = \\ &= \int_{\mathcal{L}} E_0(r) \cos kr dr \sin(kx - \omega t) - \int_{\mathcal{L}} E_0(r) \sin kr dr \cos(kx - \omega t) = \\ &= \mathcal{E}(k) \sin(kx - \omega t) \end{aligned} \quad (143)$$

Averaging integrals that involve weights $A_0(r)$ and $H_0(r)$ are evaluated similarly, and the same procedure can be used if the sine function is replaced by the cosine. The potential energy spatially averaged over one wave length consists of the following three contributions:

$$\begin{aligned} \bar{\Psi}_E &= \frac{k}{2\pi} \int_0^{\frac{2\pi}{k}} \frac{1}{2} k^2 \hat{u}^2 \left(\int_{\mathcal{L}} E_0(x - \xi) \sin(k\xi - \omega t) d\xi \right) \sin(kx - \omega t) dx = \frac{1}{4\pi} k^3 \hat{u}^2 \mathcal{E}(k) \int_0^{\frac{2\pi}{k}} \sin^2(kx - \omega t) dx = \\ &= \frac{1}{4} k^2 \hat{u}^2 \mathcal{E}(k) \end{aligned} \quad (144)$$

$$\bar{\Psi}_A = \frac{k}{2\pi} \int_0^{\frac{2\pi}{k}} \frac{1}{2} k^2 X^2 \hat{u}^2 \left(\int_{\mathcal{L}} A_0(x - \xi) \cos(k\xi - \omega t) d\xi \right) \cos(kx - \omega t) dx = \frac{1}{4} k^2 X^2 \hat{u}^2 \mathcal{A}(k) \quad (145)$$

$$\bar{\Psi}_H = \frac{k}{2\pi} \int_0^{\frac{2\pi}{k}} \frac{1}{2} (k\hat{u} - X\hat{u})^2 \left(\int_{\mathcal{L}} H_0(x - \xi) \sin(k\xi - \omega t) d\xi \right) \sin(kx - \omega t) dx = \frac{1}{4} (k - X)^2 \hat{u}^2 \mathcal{H}(k) \quad (146)$$

It is worth noting that the spatially averaged total potential energy

$$\bar{\Psi} = \bar{\Psi}_E + \bar{\Psi}_A + \bar{\Psi}_H = \frac{\hat{u}^2}{4} \left(k^2 \mathcal{E}(k) + k^2 X^2 \mathcal{A}(k) + (k - X)^2 \mathcal{H}(k) \right) \quad (147)$$

is always equal to the spatially averaged kinetic energy given by (141). To prove that, it is sufficient to verify the identity

$$k^2\mathcal{E} + k^2X^2\mathcal{A} + (k - X)^2\mathcal{H} = (\rho + \eta X^2)\omega^2 \quad (148)$$

in which, for conciseness, the dependence of the Fourier images \mathcal{E} , \mathcal{A} and \mathcal{H} on the wave number k is not marked explicitly. If X is replaced by the expression in (138), the identity can be shown to be equivalent to the dispersion equation (28).

Relations (141) and (147) indicate that the spatial averages of the kinetic and potential energy are proportional to the square of the amplitude, which can be arbitrary. However, the relative contribution of individual terms (standard or enriching ones) is amplitude-independent and can provide further insight into the role of the enrichment. If the spatial average of kinetic energy, \bar{T} , is considered as the sum of the standard term $\bar{T}_\rho = \rho\omega^2\hat{u}^2/4$ and the micromorphic term $\bar{T}_\eta = \eta X^2\omega^2\hat{u}^2/4$, the relative contribution of the enrichment can be expressed as

$$\frac{\bar{T}_\eta}{\bar{T}_\rho + \bar{T}_\eta} = \frac{\eta X^2}{\rho + \eta X^2} = \frac{l^2 X^2}{1 + l^2 X^2} = \frac{\tilde{X}^2}{1 + \tilde{X}^2} \quad (149)$$

where $\tilde{X} = lX$ is the dimensionless counterpart of X , i.e., of the ratio between the amplitudes of the micromorphic strain and of the displacement. Based on (138) and (33) converted to the dimensionless form, it is possible to show that

$$\tilde{X} = \tilde{k} \frac{\tilde{\omega}_1^2 + \tilde{\omega}_2^2 - (1 + 1/\tilde{k}^2)\tilde{\omega}^2 + (1 - \gamma\tilde{k}^2)\tilde{\mathcal{E}}}{\tilde{\omega}_1^2 + \tilde{\omega}_2^2 - (1 + \gamma)\tilde{k}^2\tilde{\mathcal{E}}} \quad (150)$$

where $\tilde{\mathcal{E}}$ can also be written in terms of \tilde{k} , $\tilde{\omega}_1$, $\tilde{\omega}_2$ and γ ; see (55). When (150) is evaluated for a specific branch of the dispersion diagram (acoustic or optical), $\tilde{\omega}$ should be understood as the frequency on that branch, but the sum $\tilde{\omega}_1^2 + \tilde{\omega}_2^2$ contains contributions of both branches and remains the same.

4.2. Example: double-mass-spring chain with nearest-neighbor interactions

For illustration, Figures 21–22 show the relative contributions of the standard and micromorphic kinetic energy terms for a range of wave numbers, separately for the acoustic and optical branches. The graphs reveal that, for a given set of parameters, the curves are the same for the acoustic and optical branch, only their meaning is flipped. This is a consequence of the fact that the amplitude ratios X_1 and X_2 evaluated for the acoustic and optical branches, respectively, satisfy the condition $X_1 X_2 = -\rho/\eta$, which then leads to $\tilde{X}_1^2 = 1/\tilde{X}_2^2$ and, consequently, to

$$\frac{\bar{T}_{\eta 1}}{\bar{T}_{\rho 1} + \bar{T}_{\eta 1}} = \frac{\tilde{X}_1^2}{1 + \tilde{X}_1^2} = \frac{1/\tilde{X}_2^2}{1 + 1/\tilde{X}_2^2} = \frac{1}{1 + \tilde{X}_2^2} = \frac{\bar{T}_{\rho 2}}{\bar{T}_{\rho 2} + \bar{T}_{\eta 2}} \quad (151)$$

As seen in Figures 21–22, for the acoustic branch, the kinetic energy of long waves (with small wave numbers) is dominated by the standard term (red curve) and the kinetic energy of short waves by the micromorphic term (blue curve), while for the optical branch it is the contrary.

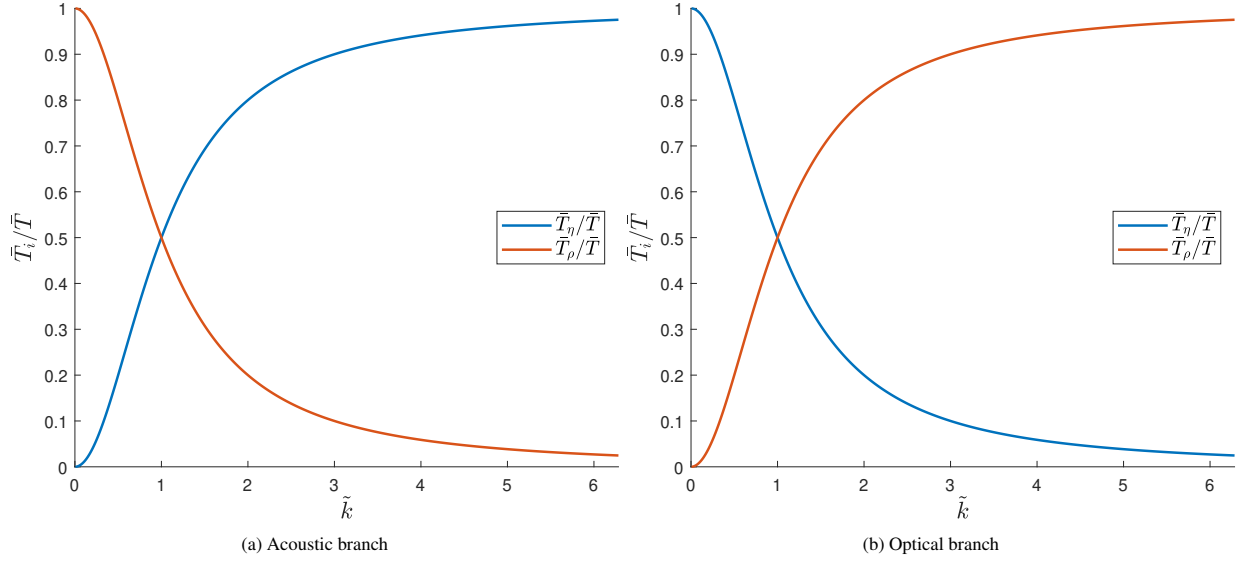


Figure 21: Relative kinetic energy contributions for parameters $\beta = 0.5$, $\gamma = 1$ and $\lambda = 1$

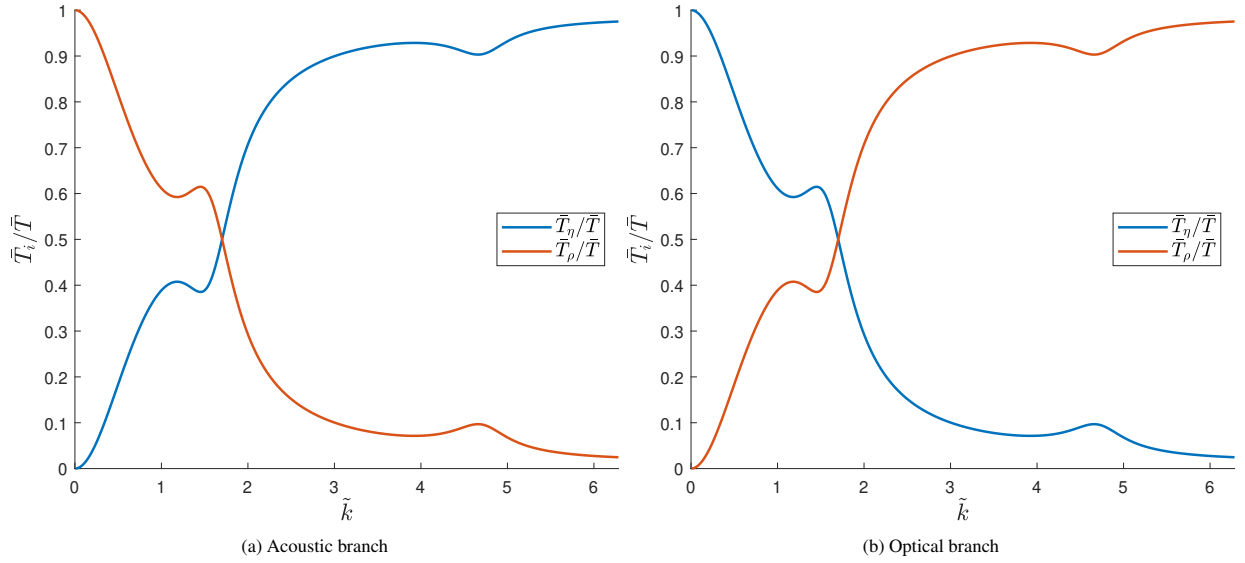


Figure 22: Relative kinetic energy contributions for parameters $\beta = 0.5$, $\gamma = 2$ and $\lambda = 1$

Similarly, we can evaluate the relative importance of three terms in the nonlocal expression for potential energy. The ratios

$$\frac{\bar{\Psi}_E}{\bar{\Psi}} = \frac{\bar{\Psi}_E}{\bar{T}} = \frac{k^2 \mathcal{E}}{(\rho + \eta X^2) \omega^2} = \frac{\tilde{k}^2 \tilde{\mathcal{E}}}{(1 + \tilde{X}^2) \tilde{\omega}^2} \quad (152)$$

$$\frac{\bar{\Psi}_A}{\bar{\Psi}} = \frac{\bar{\Psi}_A}{\bar{T}} = \frac{k^2 X^2 \mathcal{A}}{(\rho + \eta X^2) \omega^2} = \frac{\gamma \tilde{k}^2 \tilde{X}^2 \tilde{\mathcal{A}}}{(1 + \tilde{X}^2) \tilde{\omega}^2} \quad (153)$$

characterize the relative contribution of the nonlocal strain term and the nonlocal micromorphic strain gradient term; the relative contribution of the nonlocal coupling term is the complement to 1, as shown in Figures 23–24. For the acoustic branch (parts (a) of these figures), the potential energy stored in the coupling term (orange curve) is very

small and, for $\gamma = 1$, it even vanishes. On the other hand, for the optical branch it is the dominant one. Furthermore, for the acoustic branch, the strain energy (blue curve) dominates for small wave numbers and the energy stored in the gradients of micromorphic strain (red curve) dominates for large wave numbers. For the optical branch, both of these energy terms are negligible for small wave numbers and their relative contribution is the largest near $\tilde{k} = \pi/2$.

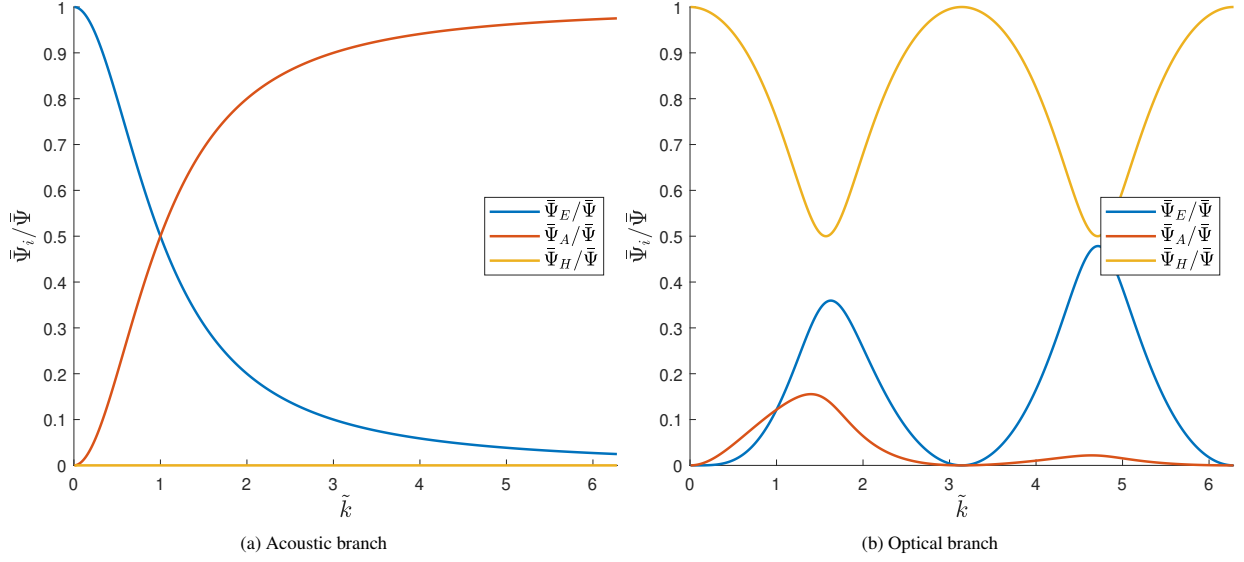


Figure 23: Relative contributions to potential energy for parameters $\beta = 0.5$, $\gamma = 1$ and $\lambda = 1$

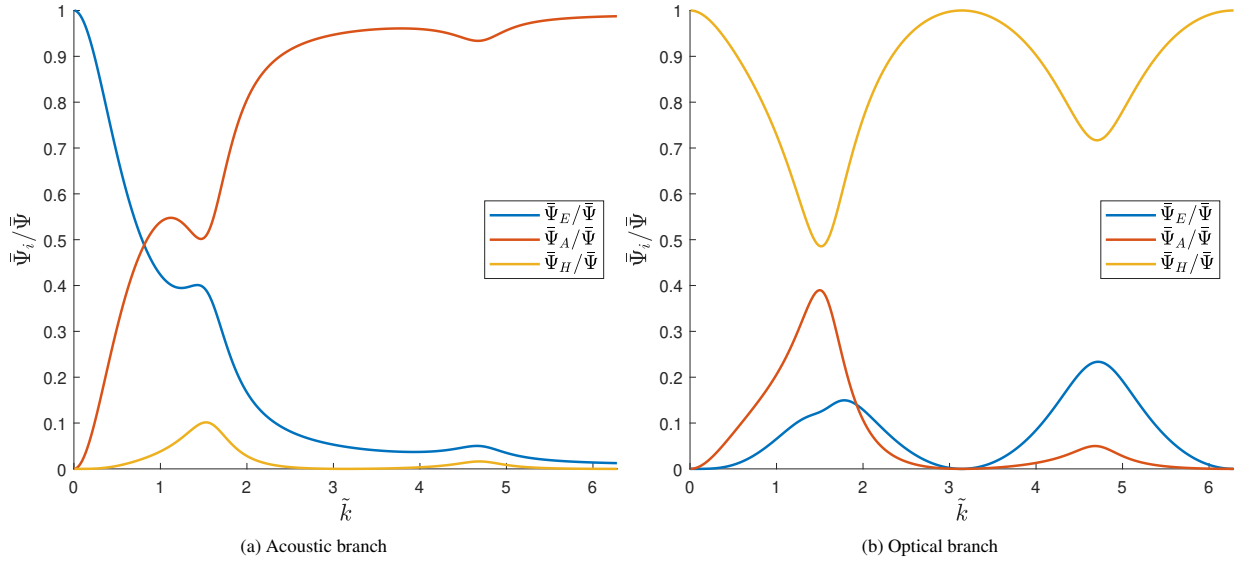


Figure 24: Relative contributions to potential energy for parameters $\beta = 0.5$, $\gamma = 2$ and $\lambda = 1$

5. Summary and Conclusions

We designed a one-dimensional micromorphic integral continuum model that can exactly reproduce the dispersion behavior of an arbitrary material with a dispersion diagram consisting of two branches, including cases when a band gap separates the branches. The proposed model enhances the classical micromorphic model by nonlocal effects

introduced into all three terms in the free energy density function. Furthermore, we developed a procedure that directly constructs the corresponding three weight functions based on the given dispersion relation describing two given branches of the dispersion diagram.

It was shown that for each dimensionless wave number \tilde{k} , the values of the dimensionless Fourier images of weight functions $\tilde{\mathcal{E}}(\tilde{k})$ and $\tilde{\mathcal{A}}(\tilde{k})$ must satisfy a quadratic equation that graphically corresponds to an ellipse in the $\tilde{\mathcal{E}} - \tilde{\mathcal{A}}$ plane. The value of the Fourier image of the third weight function $\tilde{\mathcal{H}}(\tilde{k})$ is subsequently computed from $\tilde{\mathcal{E}}(\tilde{k})$ and $\tilde{\mathcal{A}}(\tilde{k})$. Therefore, there is additional flexibility in the determination of the three weight functions, e.g., two of them can be chosen to be proportional. From the Fourier images, the original functions in the space domain are obtained by inverse Fourier transform, which needs to be performed numerically and constitutes the only source of potential error.

In the results section, the developed identification procedure was applied to simple discrete models, which can simulate, e.g., atomic interactions. A mass-spring chain with two alternating masses is perhaps one of the simplest models for which a band gap in the dispersion curve is observed and hence is chosen as the basic toy problem. To keep the two functions $\tilde{\mathcal{E}}$ and $\tilde{\mathcal{A}}$ proportional and simultaneously ensure that both are real, the proportionality constant must be chosen within certain limits. This feature is nicely visualized when the ellipses depicting the set of possible solutions are plotted. It was also shown that, in this basic case, the nonlocality needs to be present in all three terms in the free energy density function, meaning that none of the weight functions can be chosen as a multiple of the Dirac delta distribution. The obtained weight functions are real, finite valued, and of reasonable shapes. The deviations between the dispersion diagram acquired with the proposed enriched continuum model using the approximated weight functions and the analytical one increase for larger wave numbers. The error is exclusively due to the numerical evaluation of the inverse Fourier transform, and it can be made arbitrarily small by increasing the number of sampling points and the length of the sampling window. In the special case of a mass-spring chain with equal masses, analytical expressions for the weight functions are obtained when the two functions $\tilde{\mathcal{E}}$ and $\tilde{\mathcal{A}}$ are enforced to be identical.

A slightly more complex dispersion diagram is obtained when second-neighbour interactions are added to the basic double-mass-spring chain model. Also for this test case, the weight functions are reasonable and well-behaved.

The last example was focused on the dispersion behavior of the local micromorphic model with vanishing micromorphic stiffness, which is the only case in which the local model exhibits a band gap. Using the proposed methodology, one obvious solution can be obtained when the weight function $\tilde{\mathcal{A}}$ vanishes and the other two are set to multiples of the Dirac distribution, since then the nonlocal model degenerates to the local one to be reproduced. Nevertheless, additional solutions with all nonvanishing weight functions exist, and they are acquired by applying the developed procedure. The resulting functions $\tilde{\mathcal{E}}$ and $\tilde{\mathcal{A}}$ are reasonable and finite valued, but the function $\tilde{\mathcal{H}}$ contains a contribution of the Dirac distribution.

Finally, individual contributions to the energy associated with a harmonic wave were evaluated. It was shown that the spatial averages of kinetic energy and of potential energy are the same. Furthermore, the relative contribution of individual terms in the energy functional was analyzed for the acoustic and optical branches, and their importance for long and short waves was discussed. For waves that correspond to the acoustic branch, the major contribution to the kinetic energy of long waves comes from the standard term and to the potential energy of long waves from the strain-related nonlocal term. As the wave length gets comparable to the internal length of the model, the contribution of the micromorphic inertia to the kinetic energy and of the nonlocal term involving the gradient of micromorphic strain to the potential energy increases. For waves that correspond to the optical branch, the major contribution to the kinetic energy of long waves comes from the micromorphic inertia and to the potential energy of long waves from the nonlocal term that penalizes the difference between standard and micromorphic strain. As the wave length gets comparable to the internal length of the model, the contribution of the standard inertia to the kinetic energy and of the nonlocal terms involving the standard strain and the gradient of micromorphic strain to the potential energy increases.

Acknowledgements

Financial support received in 2023 from the Czech Science Foundation (project No. 19-26143X) is gratefully acknowledged. In 2024, this work was co-funded by the European Union under the ROBOPROX project (reg. no. CZ.02.01.01/00/22_008/0004590) and by MŠMT - ERC CZ project No. LL2310.

References

- [1] V. Nežerka, M. Somr, T. Janda, J. Vorel, M. Doškář, J. Antoř, J. Zeman, J. Novák, A jigsaw puzzle metamaterial concept, *Composite Structures* 202 (2018) 1275–1279.
- [2] M. Lei, W. Hong, Z. Zhao, C. Hamel, M. Chen, H. Lu, H. J. Qi, 3d printing of auxetic metamaterials with digitally reprogrammable shape, *ACS applied materials & interfaces* 11 (2019) 22768–22776.
- [3] R. V. Craster, S. Guenneau, *Acoustic metamaterials: Negative refraction, imaging, lensing and cloaking*, volume 166, Springer Science & Business Media, 2012.
- [4] G. Ma, P. Sheng, Acoustic metamaterials: From local resonances to broad horizons, *Science advances* 2 (2016) e1501595.
- [5] C. Sugino, S. Leadenham, M. Ruzzene, A. Erturk, On the mechanism of bandgap formation in locally resonant finite elastic metamaterials, *Journal of Applied Physics* 120 (2016) 134501.
- [6] A. N. Norris, Acoustic cloaking, *Acoust. Today* 11 (2015) 38–46.
- [7] M. Miniaci, A. Krushynska, F. Bosia, N. M. Pugno, Large scale mechanical metamaterials as seismic shields, *New Journal of Physics* 18 (2016) 083041.
- [8] D. Roca, D. Yago, J. Cante, O. Lloberas-Valls, J. Oliver, Computational design of locally resonant acoustic metamaterials, *Computer Methods in Applied Mechanics and Engineering* 345 (2019) 161–182.
- [9] L. Liu, A. Sridhar, M. Geers, V. Kouznetsova, Computational homogenization of locally resonant acoustic metamaterial panels towards enriched continuum beam/shell structures, *Computer Methods in Applied Mechanics and Engineering* 387 (2021) 114161.
- [10] T. F. van Nuland, P. B. Silva, A. Sridhar, M. G. Geers, V. G. Kouznetsova, Transient analysis of nonlinear locally resonant metamaterials via computational homogenization, *Mathematics and Mechanics of Solids* 24 (2019) 3136–3155.
- [11] H. Askes, A. V. Metrikine, A. V. Pichugin, T. Bennett, Four simplified gradient elasticity models for the simulation of dispersive wave propagation, *Philosophical magazine* 88 (2008) 3415–3443.
- [12] J. Fish, W. Chen, G. Nagai, Non-local dispersive model for wave propagation in heterogeneous media: one-dimensional case, *International Journal for Numerical Methods in Engineering* 54 (2002) 331–346.
- [13] A. C. Eringen, Linear theory of nonlocal elasticity and dispersion of plane waves, *International Journal of Engineering Science* 10 (1972) 425–435.
- [14] C. Lim, G. Zhang, J. Reddy, A higher-order nonlocal elasticity and strain gradient theory and its applications in wave propagation, *Journal of the Mechanics and Physics of Solids* 78 (2015) 298–313.
- [15] M. Jirásek, Nonlocal theories in continuum mechanics, *Acta Polytechnica* 44 (2004) 16–34.
- [16] A. C. Eringen, E. Suhubi, Nonlinear theory of simple micro-elastic solids—I, *International Journal of Engineering Science* 2 (1964) 189–203.
- [17] R. D. Mindlin, Microstructure in linear elasticity, *Archive for Rational Mechanics and Analysis* volume 16 (1964) 51–78.
- [18] E. Cosserat, *Théorie des corps déformables*, Librairie Scientifique A. Hermann et Fils, 1909.
- [19] G. Herrmann, J. D. Achenbach, Applications of theories of generalized cosserat continua to the dynamics of composite materials, in: *Mechanics of generalized continua*, Springer, 1968, pp. 69–79.
- [20] A. C. Eringen, Theory of thermo-microstretch elastic solids, *International Journal of Engineering Science* 28 (1990) 1291–1301.
- [21] S. Tomar, D. Singh, Propagation of stoneley waves at an interface between two microstretch elastic half-spaces, *Journal of Vibration and Control* 12 (2006) 995–1009.
- [22] A. Berezovski, J. Engelbrecht, A. Salupere, K. Tamm, T. Peets, M. Berezovski, Dispersive waves in microstructured solids, *International Journal of Solids and Structures* 50 (2013) 1981–1990.
- [23] A. Madeo, P. Neff, M. V. d’Agostino, G. Barbagallo, Complete band gaps including non-local effects occur only in the relaxed micromorphic model, *Comptes Rendus Mécanique* 344 (2016) 784–796.
- [24] A. Berezovski, M. E. Yildizdag, D. Scerrato, On the wave dispersion in microstructured solids, *Continuum Mechanics and Thermodynamics* 32 (2020) 569–588.
- [25] P. Neff, I.-D. Ghiba, A. Madeo, L. Placidi, G. Rosi, A unifying perspective: the relaxed linear micromorphic continuum, *Continuum Mechanics and Thermodynamics* 26 (2014) 639–681.
- [26] I.-D. Ghiba, P. Neff, A. Madeo, L. Placidi, G. Rosi, The relaxed linear micromorphic continuum: existence, uniqueness and continuous dependence in dynamics, *Mathematics and Mechanics of Solids* 20 (2015) 1171–1197.
- [27] A. Madeo, P. Neff, I.-D. Ghiba, L. Placidi, G. Rosi, Band gaps in the relaxed linear micromorphic continuum, *ZAMM-Journal of Applied Mathematics and Mechanics/Zeitschrift für Angewandte Mathematik und Mechanik* 95 (2015) 880–887.
- [28] P. Neff, A. Madeo, G. Barbagallo, M. V. d’Agostino, R. Abreu, I.-D. Ghiba, Real wave propagation in the isotropic-relaxed micromorphic model, *Proceedings of the Royal Society A: Mathematical, Physical and Engineering Sciences* 473 (2017) 20160790.
- [29] A. Madeo, P. Neff, E. C. Aifantis, G. Barbagallo, M. V. d’Agostino, On the role of micro-inertia in enriched continuum mechanics, *Proceedings of the Royal Society A: Mathematical, Physical and Engineering Sciences* 473 (2017) 20160722.
- [30] M. V. d’Agostino, G. Barbagallo, I.-D. Ghiba, B. Eidel, P. Neff, A. Madeo, Effective description of anisotropic wave dispersion in mechanical band-gap metamaterials via the relaxed micromorphic model, *Journal of elasticity* 139 (2020) 299–329.
- [31] I.-D. Ghiba, P. Neff, S. Owczarek, Existence results for non-homogeneous boundary conditions in the relaxed micromorphic model, *Mathematical Methods in the Applied Sciences* 44 (2021) 2040–2049.

- [32] N. NejadSadeghi, A. Misra, Role of higher-order inertia in modulating elastic wave dispersion in materials with granular microstructure, *International Journal of Mechanical Sciences* 185 (2020) 105867.
- [33] M. El Sherbiny, L. Placidi, Discrete and continuous aspects of some metamaterial elastic structures with band gaps, *Arch Appl Mech* 88 (2018) 1725—1742.
- [34] L. Placidi, M. G. El Sherbiny, P. Baragatti, Experimental investigation for the existence of frequency band gap in a microstructure model, *Mathematics and Mechanics of Complex Systems* 9 (2021) 413–421.
- [35] M. Jirásek, M. Horák, M. Šmejkal, Integral micromorphic model for band gap in 1d continuum, *Continuum Mechanics and Thermodynamics* (2023) 1–20.
- [36] L. Placidi, F. Di Girolamo, R. Fedele, Variational study of a maxwell–rayleigh-type finite length model for the preliminary design of a tensegrity chain with a tunable band gap, *Mechanics Research Communications* 136 (2024) 104255.
- [37] H. Askes, A. V. Metrikine, Higher-order continua derived from discrete media: continualisation aspects and boundary conditions, *International Journal of Solids and Structures* 42 (2005) 187–202.
- [38] A. Bacigalupo, L. Gambarotta, Generalized micropolar continualization of 1d beam lattices, *International Journal of Mechanical Sciences* 155 (2019) 554–570.
- [39] A. Bacigalupo, L. Gambarotta, A dynamic high-frequency consistent continualization of beam-lattice materials, *Composite Structures* 272 (2021) 114146.
- [40] V. Diana, A. Bacigalupo, L. Gambarotta, Thermodynamically-consistent dynamic continualization of block-lattice materials, *International Journal of Solids and Structures* 262 (2023) 112050.
- [41] T. Roubíček, Some gradient theories in linear visco-elastodynamics towards dispersion and attenuation of waves in relation to large-strain models, *Acta Mechanica* (2024) 1–25.
- [42] N. W. Ashcroft, N. D. Mermin, *Solid State Physics*, 1st ed., Cengage Learning, 1976.